



January 2016

# Remote Sensing Of Asteroid Surface Mineralogy

Martin William Hynes

Follow this and additional works at: <https://commons.und.edu/theses>

---

## Recommended Citation

Hynes, Martin William, "Remote Sensing Of Asteroid Surface Mineralogy" (2016). *Theses and Dissertations*. 2028.  
<https://commons.und.edu/theses/2028>

This Thesis is brought to you for free and open access by the Theses, Dissertations, and Senior Projects at UND Scholarly Commons. It has been accepted for inclusion in Theses and Dissertations by an authorized administrator of UND Scholarly Commons. For more information, please contact [zeinebyousif@library.und.edu](mailto:zeinebyousif@library.und.edu).

**REMOTE SENSING OF ASTEROID SURFACE MINERALOGY**

**by**

**Martin William Hynes**

**Bachelor of Science, National University of Ireland, Galway 1995**

**A Thesis**

**Submitted to the Graduate Faculty**

**of the**

**University of North Dakota**

**In partial fulfillment of the requirements**

**for the degree of**

**Master of Science**

**Grand Forks, North Dakota**

**December**

**2016**

Title            Remote Sensing of Asteroid Surface Mineralogy

Department    Space Studies

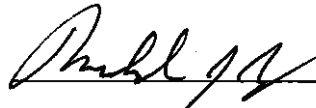
Degree         Master of Science

In presenting this thesis in partial fulfillment of the requirements for a graduate degree from the University of North Dakota, I agree that the library of this University shall make it freely available for inspection. I further agree that permission for extensive copying for scholarly purposes may be granted by the professor who supervised my (thesis or dissertation) work or, in her/his absence, by the Chairperson of the department or the dean of the Graduate School. It is understood that any copying or publication or other use of this thesis -or part thereof for financial gain shall not be allowed without my written permission. It is also understood that due recognition shall be given to me and to the University of North Dakota in any scholarly use which may be made of any material in my thesis.

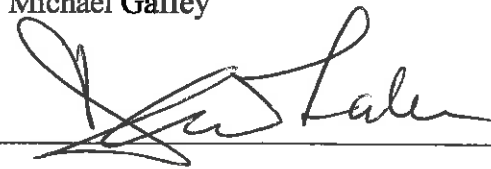
Martin William Hynes

December 2016

This thesis submitted by Martin Hynes in partial fulfillment of the requirements for the Degree of Master of Science in Space Studies has been read by the Faculty Advisory Committee under whom the work has been done, and is hereby approved.

 10/26/16

Dr. Michael Gaffey



Dr. David Whalen



Dr. Paul Hardersen

This thesis is being submitted by the appointed advisory committee as having met all of the requirements of the Graduate School at the University of North Dakota and is hereby approved.



Grant McGimpsey, PhD  
Dean of the Graduate School

November 2, 2016

Date

## TABLE OF CONTENTS

|  |    |
|--|----|
| LIST OF FIGURES .....                                  | v  |
| LIST OF TABLES .....                                   | ix |
| ACKNOWLEDGMENTS .....                                  | x  |
| ABSTRACT .....   | xi |
| CHAPTER  |    |
| I.    INTRODUCTION.....                                | 1  |
| II.   DYNAMIC EVOLUTION OF ASTEROID ORBITS.....        | 10 |
| III.  MINERALOGICAL ANALYSIS OF ASTEROID SURFACES...27 |    |
| IV.  OBSERVATIONS AND DATA REDUCTION.....              | 43 |
| V.   DATA ANALYSIS AND RESULTS.....                    | 56 |
| VI.  CONCLUSIONS AND RECOMMENDATIONS.....              | 72 |
| APPENDICES.....  | 74 |
| REFERENCES .....                                       | 81 |

## LIST OF FIGURES

| Figure |  | Page |
|--------|--|------|
| 1.1    | Fireball in the Jovian atmosphere which resulted from the impact of comet Shoemaker Levy 9   | 2    |
| 1.2    | Average impact frequency as a function of impact energy                                      | 3    |
| 1.3    | Light Curve for 3628 Božněmcová (Warner, 2008)   | 7    |
| 2.1    | Location of the Main Asteroid Belt   | 10   |
| 2.2    | Orbital Parameters   | 11   |
| 2.3    | Distribution of asteroid orbital eccentricities  | 12   |
| 2.4    | Distribution of asteroid orbital inclinations  | 13   |
| 2.5    | The Kirkwood Gaps  | 14   |
| 2.6    | Orbit of 433 Eros  | 15   |
| 2.7    | Location of the secular resonances in the asteroid belt                                      | 18   |
| 2.8    | (a) The diurnal Yarkovsky effect, (b) The seasonal Yarkovsky effect                          | 23   |
| 2.9    | Detection of the Yarkovsky effect on near-Earth asteroid 6489 Golevka. Chesley et al (2003). | 23   |
| 2.10   | YORP induced spin-up of an asymmetrical asteroid. (Rubincam 2000)                            | 25   |
| 2.11   | Direct detection of the YORP effect in near-Earth asteroid, 2000 PH5 (Lowry et al., 2007)    | 26   |
| 3.1    | Shape of the d sub shells (USGS)   | 29   |

| Figure | Page  |    |
|--------|---|----|
| 3.2    | Relative energy levels of the d sub shells of a transition metal as a free ion, an unperturbed ion in a crystal field and split due to an octahedral crystal field (Burns 1970) | 30 |
| 3.3    | Interaction between a photon and an electron in a mineral crystal   | 31 |
| 3.4    | Reflectance spectra of asteroid 4 Vesta compared with a lunar sample and various meteorites. (McCord et al 1970)  | 33 |
| 3.5    | Crystal structure of Diopside, a monoclinic pyroxene mineral (USGS)   | 35 |
| 3.6    | 3d orbital energy level diagrams for Fe <sup>2+</sup> ions in orthoferrosilite. (Burns, 1985a)  | 36 |
| 3.7    | 3d orbital energy level diagram for Fe <sup>2+</sup> ion in fayalite. (Burns, 1985a)  | 36 |
| 3.8    | Mineralogical variation in the S-asteroid subtypes. (Gaffey et al, 1993)  | 42 |
| 4.1    | Atmospheric transmission at the summit of Mauna Kea for the wavelength range 0.9 to 2.7μm. (Tom Geballe, Gemini Observatory).   | 43 |
| 4.2    | Schematic of the Spex Instrument (NASA IRTF)  | 45 |
| 4.3    | FITS image showing the raw spectrum of asteroid 2002JB <sub>9</sub>   | 47 |
| 4.4    | IRAF plot of raw pixel count (flux) verses channel number   | 47 |
| 4.5    | Determination of the aperture center using the IRAF <i>apall</i> routine  | 48 |
| 4.6    | Argon emission line spectra captured on the spectrograph array  | 49 |
| 4.7    | Raw Spectrum of Asteroid 3628 Božněmcová  | 50 |
| 4.8    | Plot of the log of extinction star flux verse air mass  | 51 |

| Figure  | Page |
|---|------|
| 4.9 Spec PR plot showing the effect of progressively channel shifting the standard star spectra by 1/10 of a channel.               | 52   |
| 4.10 Slope of the starpack used to remove telluric features from 3628 Božněmcová  | 52   |
| 4.11 Resulting averaged spectrum of 3628 Božněmcová divided by starpack   | 53   |
| 4.12 Averaged Spectral Flux curve of Solar Analog Star SAO 157621   | 54   |
| 4.13 Solar Analog Star/Divided by Starpack.   | 54   |
| 4.14 Final reflectance spectrum of asteroid 3628 Božněmcová   | 55   |
| 5.1 Diagnostic Spectral Parameters from <i>Mineralogy of Asteroids</i> (Gaffey 2001)  | 56   |
| 5.2 Combined Hynes 2011 and SMASS spectrum for 3628 Božněmcová  | 57   |
| 5.3 Linear continuum fit to the Band 1 feature of 3628 Božněmcová   | 58   |
| 5.4 Linear continuum fit to the Band 2 feature of 3628 Božněmcová   | 58   |
| 5.5 Polynomial fit to the 1 micron feature  | 59   |
| 5.6 Polynomial fit to the 2 micron feature  | 59   |
| 5.7 Visible/near IR spectrum of 3628 Božněmcová compared to spectra of ordinary chondrite meteorites. (Binzel et al, 1993)          | 61   |
| 5.8 Normalized reflectance spectrum of 3628 Božněmcová compared to an LL6 ordinary chondrite. (Burbine & Binzel 2002)               | 62   |
| 5.9 Laboratory reflectance spectra (0.3–2.6 $\mu\text{m}$ ) of three pairs of type A and type B clinopyroxenes (Cloutis et al 2006) | 63   |



| Figure   | Page |
|--|------|
| 5.10 Spectra of angrite meteorites. (Burbine et, 2001).        | 65   |
| 5.11 Comparison of Angra Dos Reis & Božněmcová spectra         | 65   |
| 5.12 Band 1 verse Band 2 plot of Božněmcová and Angra Dos Reis | 67   |
| 5.13 Observing log for 2002JB9                                 | 68   |
| 5.14 Spectrum of NEA 2002 JB9                                  | 69   |
| 5.15 Solar phase curve for 2002JB9 (Hicks et al., 2011).       | 70   |

## LIST OF TABLES

| Table |   | Page |
|-------|---|------|
| 1.    | Relationship of asteroid and meteorite classification schemes | 51   |

## ACKNOWLEDGMENTS

I wish to express my sincere appreciation to the members of my advisory committee for their guidance and support during my time in the Space Studies program at the University of North Dakota. I would also like to thank Dr. Sherry Fieber-Beyer, Dr. Vishnu Reddy and Ms. Jessica Blagen for their support.

Research for this thesis was supported by NASA Near Earth Object Observation Program grant NNX07AL29G.

## ABSTRACT

A major research question in asteroid science centres on how fragments from main belt asteroids, which are located between the orbits of Mars and Jupiter, end up in Earth crossing orbits. Advances in infrared astronomy have made it possible to test the validity of solar system dynamical models using observational data. Specifically, near-infrared (NIR) reflectance spectroscopy can be employed to search the main asteroid belt for possible mineralogical analogues of Near Earth asteroids. Two asteroids, 3628 Božněmcová and 2002 JB<sub>9</sub>, were studied using the NASA Infrared Telescope Facility. 3628 Božněmcová had been suggested as a possible parent body for ordinary chondrite meteorites due to its unique spectral characteristics and the fact that it orbits in the vicinity of the 3:1 Kirkwood gap. A more recent suggestion by Cloutis et al. (2006) is that 3628 Božněmcová is a type A clinopyroxene and possible parent body for the angrite meteorites.

The spectrum of 3628 Božněmcová obtained during the observing run of June 2011 shows distinct absorption features at 1.02 and 2.16 microns. It is therefore possible to effectively rule out an ordinary chondrite or howardite-eucrite-diogenite (HED) mineralogy for this asteroid. While not entirely conclusive, the implied mineralogy for 3628 Božněmcová, i.e., a high calcium type B clinopyroxene with a possible fassite component, suggests it may be a possible parent body for the angrite meteorites.

## **Chapter I**

### **Introduction**

In early July 1994 comet Shoemaker-Levy 9 was in the process of disintegrating, being literally ripped apart by Jupiter's immense gravitational field. Soon after, fragments of the comet began to enter the Jovian atmosphere. The impact of Fragment G produced a fire ball larger than the Earth and estimated to have been equivalent to detonating six billion megatons of TNT (Bruton, 1994). Figure 1.1, a near infrared image at 2.34 microns taken by McGregor using the 2.3 meter telescope at Siding Spring observatory, Australia, shows the fireball in Jupiter's atmosphere 12 minutes after the impact. Crater evidence on the surfaces of the rocky terrestrial planets demonstrates that this is definitely not the first time such a violent impact has occurred and should serve as a reminder that we live in a dynamic solar system.

It is now widely accepted that an asteroid impact was most likely responsible for the Cretaceous-Tertiary Mass Extinction event. In a classic example of "punctuated equilibrium" seventy five percent of the species on the Earth at the time were wiped out by a single impact. The work of Alvarez et al. (1980) and the subsequent discovery of the Chicxulub impact crater off the Yucatan peninsula led to a gradual realization of the dangers posed by asteroid impacts.

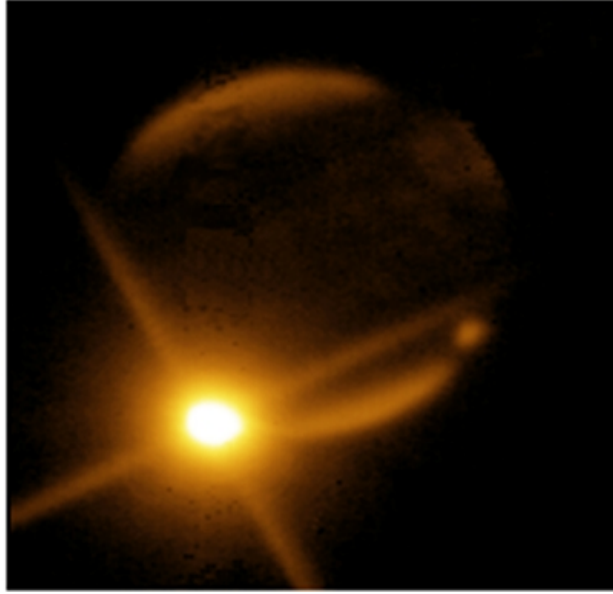


**Figure 1.1** Fragment G, comet Shoemaker-Levy 9, explodes in Jupiter's atmosphere (McGregor, 1994).

The potential scale of destruction resulting from an asteroid impact is largely a function the object's kinetic energy and composition. The kinetic energy can be calculated from the following simple equation:

$$e = \frac{1}{2} mv^2 \quad \text{where } m \text{ is the asteroid's mass and } v \text{ is its impact velocity.} \quad \textbf{Equation 1}$$

The mass of an asteroid is a function of its density and volume. The impact energy can be expressed in megatons of TNT (Morbidelli et al., 2002) if the kinetic energy equation is re-written as:

$$e = 62.5 \rho d^3 v^2 \quad \text{where energy is in megatons, } \rho \text{ (density) is in } g/cm^3, d \text{ (diameter) is in kilometers, and velocity is in } km/s. \quad \textbf{Equation 2}$$

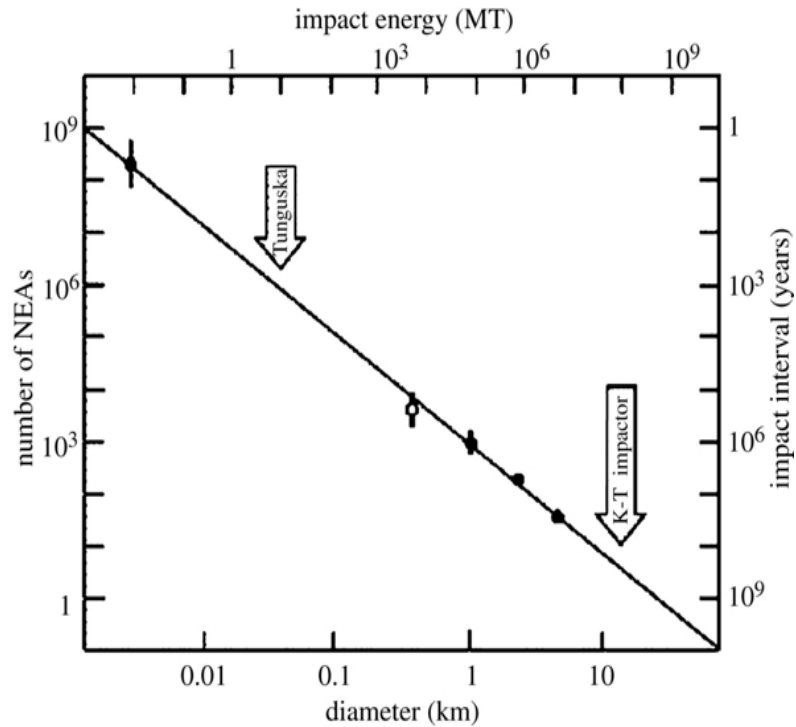


**Figure 1.2 Average impact frequency as a function of asteroid diameter (Morrison, 2006)**

Figure 1.2 from Morrison (2006) shows a plot of the average impact frequency for asteroids of various diameters. The first data point at the upper left side of the plot is an estimate derived from observations of bright bolides in the upper atmosphere. The four data points in the lower right quadrant show asteroid diameters ranging from 30 meters to 5 kilometers, which are representative of asteroids in near-Earth orbits (Morrison, 2006). The data seems to imply that, statistically, the Earth is struck roughly once every one to two hundred years by an asteroid capable of destroying a large metropolitan area. Anecdotal evidence suggests that this may well be the case. In 1908 an asteroid broke up in the atmosphere over the Tunguska region of Russia. The resulting air burst, estimated to be in the 10 to 20 megaton range, destroyed over 2000 km<sup>2</sup> of forest. Had this object arrived several hours later, further west, the history of twentieth century Northern Europe may have been radically different. The recent February 2013 airburst over the

Chelyabinsk region of Russia, while not of the same magnitude, seems to correlate with the basic size versus frequency trend.

The 1992 *Spaceguard Survey* report directed NASA to search for potential Earth impactors 1 kilometer or greater in diameter. The heightened awareness following the 1994 Shoemaker-Levy impacts prompted the US Congress to act resulting in the *Spaceguard Survey* receiving a much higher priority. It was followed in 2005 by the *George E. Brown, Jr. Near-Earth Object Survey Act* (H.R. 1022, 109<sup>th</sup>) which mandates that NASA “*detect, track, catalog and characterize near-Earth asteroids (and comets) in order to provide warning and mitigation of the potential hazard of such objects to the Earth*”. This new legislation also pushes the detection limit down from the initial 1 kilometer diameter of *Spaceguard* to 140 meters.

The motivation for my research is threefold. First is the desire to understand the mineralogical composition of Near Earth Asteroids. This knowledge is vital to any future impact risk mitigation mission for the simple reason that the optimum strategy to deflect or destroy a potentially hazardous asteroid is very much dependent on its physical nature. Consider for example a deflection strategy that involves detonating a nuclear device in close proximity to an asteroid. This may well succeed if the asteroid is a solid metallic body, however, if the asteroid were highly porous or a loose, gravitationally bound, aggregate it is likely that most of the blast energy would simply be absorbed. The end result is that the asteroid may remain largely intact with its orbit essentially unaltered and would thus continue to pose a threat to the Earth. There is also the possibility that the asteroid may be disrupted into many fragments, but with an insufficient change in its orbit.



Sending a robotic spacecraft rendezvous mission to perform an in-situ mineralogical characterization of an asteroid's surface is an extremely complex, risky and expensive proposition. To date only two spacecraft have actually landed on an asteroid. NASA's Near Earth Asteroid Rendezvous (NEAR) spacecraft landed on asteroid 433 *Eros* in 2001 and took gamma ray measurements which provided elemental abundance but not surface mineralogy. The on board Near Infrared Spectrometer (NIS) instrument obtained more than 200,000 reflectance spectra (800 to 2500 nm) during the approach and departure from the asteroid (Bell et al. 2001). The total cost of the mission was \$224 million. The Japanese *Hayabusa* spacecraft visited asteroid *Itokawa* in 2005 and returned approximately 1500 microscopic grains of surface material to Earth six years later (Nakamura et al. 2010). Synchrotron-radiation x-ray diffraction and scanning electron microscope analysis indicated that the mineralogy of the particles was identical to those of thermally metamorphosed LL chondrite meteorites (Nakamura et al. 2010). This mission cost \$170 million (JAXA).

A far less costly alternative is to utilize ground based remote sensing to measure the asteroid's reflectance spectra. Asteroids are actually well suited for remote geochemical analysis because their spectral features are especially sensitive to variations in mineral composition. Many asteroid surfaces are composed of the same silicate materials (olivine, pyroxene, etc.) that form the crust of the terrestrial planets. These silicate minerals contain relatively high abundances of transition series elements, especially iron. Absorption of incident photons of infrared light by transition series

cations produces spectral absorption features<sup>1</sup> which are diagnostic of mineralogy (although this is not possible with every mineral). Mineralogical characterizations are possible provided the spectra have sufficient wavelength coverage, resolution, and a high enough signal to noise ratio to allow accurate extraction of diagnostic spectral parameters (Gaffey et al. 2002). The silicate mineralogy of an asteroid surface is heavily dependent on the formation environment and thermal history of the body so once an understanding of the mineralogical composition has been gained it is possible to place constraints on the possible formation scenarios that produced an asteroid.

A number of criteria were used in selecting which asteroids to observe during our allocated time on NASA's Infrared Telescope Facility (IRTF). Chief amongst these was that targets considered for observation needed to have an apparent magnitude of 17 or brighter<sup>2</sup> in order to provide a useful signal to noise ratio. Additionally, to minimize the effects of atmospheric absorption, targets closer to zenith were preferable.

A desire to understand the orbital dynamics at play in the asteroid belt is the second motivation for this work. Near Earth asteroids are believed to be fragments of larger parent bodies located in the main asteroid belt and an important goal in asteroid science is to understand the delivery mechanisms which transport these fragments from the main asteroid belt into near Earth orbits. Comparative spectroscopy, specifically the detection of diagnostic absorption features, can be employed to test for possible Near Earth Asteroid mineralogical analogues in the main belt. By forging links between Main Belt asteroids, near-Earth asteroids, and meteorites it is possible to reconstruct the

---

<sup>1</sup> The Fe<sup>2+</sup> cation is responsible for the dominant absorptions features in the visible and near-infrared..

<sup>2</sup> Asteroids are brightest when observed at opposition from the sun.

dynamic and petrogenetic processes operating in the inner part of the solar system (Cloutis et al. 2006).

A search of the known main belt and near Earth asteroid population produced a list from which targets meeting the criteria discussed above were identified. The two asteroids chosen for analysis were 3628 Božněmcová and 2002 JB<sub>9</sub>. 3628 Božněmcová was discovered in 1979 by Czech astronomer Zdenka Vávrová and has an estimated diameter of 7 kilometers. It is of interest due to the fact that it orbits near the 3:1 Kirkwood gap which is predicted to be a source of Near Earth objects. Warner (2008) measured the light curve of 3628 Božněmcová (see figure 1.3) and derived a rotation period of 3.33541 hours  $\pm$  0.000057 h.

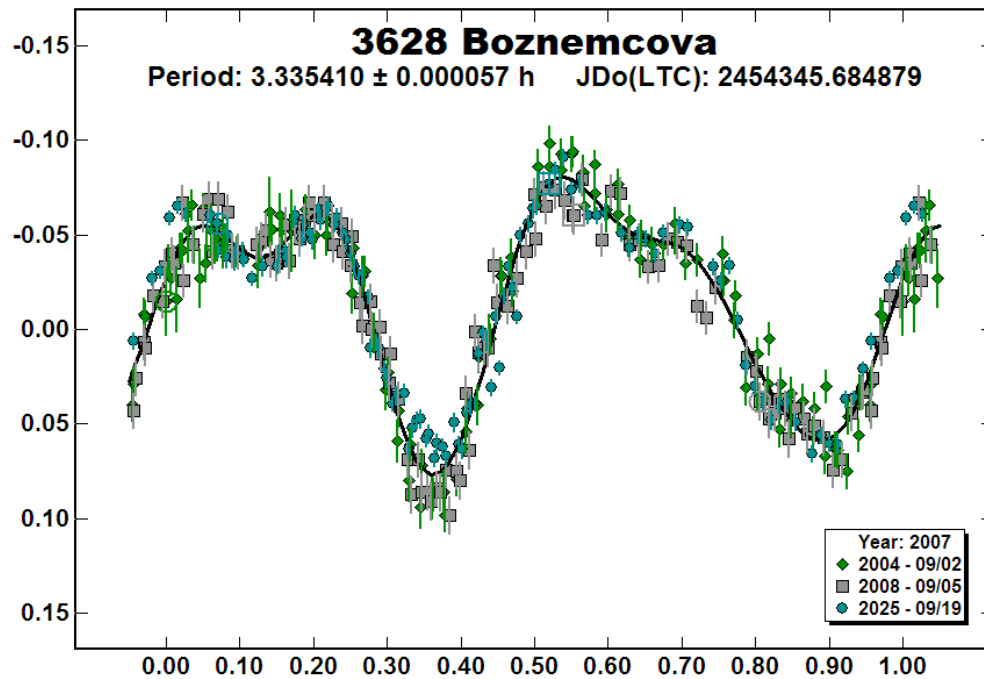


Figure 1.3 Light Curve for 3628 Božněmcová (Warner, 2008)

2002 JB<sub>9</sub> discovered by the Lincoln Near-Earth Asteroid Research (LINEAR) survey has been identified by the Minor Planet Center as a potentially hazardous asteroid. A Potentially Hazardous Asteroid (PHA) is defined as an Near Earth asteroid whose Minimum Orbit Intersection Distance (MOID) with the Earth is 0.05 AU or less and whose absolute magnitude (H) is 22.0 or brighter. The MOID for 2002 JB<sub>9</sub> is a mere 0.034 AU (5086327 km). The absolute magnitude (H) is 15.684 Its orbital elements are actually quite similar to a Jupiter-family comet (appendix 2). The likelihood of collision increases as the asteroid's orbit becomes more coplanar with the Earth's orbit. 2002 JB<sub>9</sub> is a fast rotator with a period of 2.4261 hours, which suggests that it is probably not a loosely bound rubble pile as the centrifugal forces would cause it to disintegrate (Gaffey, 2010 lecture). I will investigate if a link can be established between NEA 2002 JB<sub>9</sub> and either a parent body in the main asteroid belt or a meteorite specimen.

The third motivation for this research is the desire to understand the chemical and thermal environment of the early inner solar system. Asteroids are the remnants of the primitive solar nebula materials from which the terrestrial planets formed. Preserved in their primitive state, asteroids represent the best forensic evidence available with which to study the formation and early thermal history of the inner solar system. "It is known that all significant chemical processes that affected the minor planets were essentially complete within the first 0.5% of solar system history" (Gaffey et al. 2002). The most ancient igneous meteorites in the terrestrial collection are the angrites which have crystallization ages of 4.55 billion years (Burbine et al. 2006). Angrites are generally believed to be fragments of a basaltic asteroid that differentiated under relatively oxidizing conditions (Burbine et al. 2006). To date no known parent body has

been identified. It has been suggested that 3628 Božněmcová may be the parent body of the angrite meteorites (Cloutis et al 2006). I propose to use NIR reflectance spectroscopy to test this hypothesis. Identification of a parent body will enable us to better understand the early history of the inner solar system by placing constraints on the timing of differentiation in the asteroid belt.

## Chapter II

### Dynamic Evolution of Asteroid Orbits

The main asteroid belt, located between the orbits of Mars and Jupiter (Figure 2.1) is believed to be the source of most Near Earth Asteroids (Bottke et al. 2000). It is estimated that there are currently over one million objects, with diameters greater than one kilometer, in the belt (Petit et al. 2001). This chapter will review the mechanisms which are thought to be responsible for moving asteroids from the main belt into near Earth orbits.

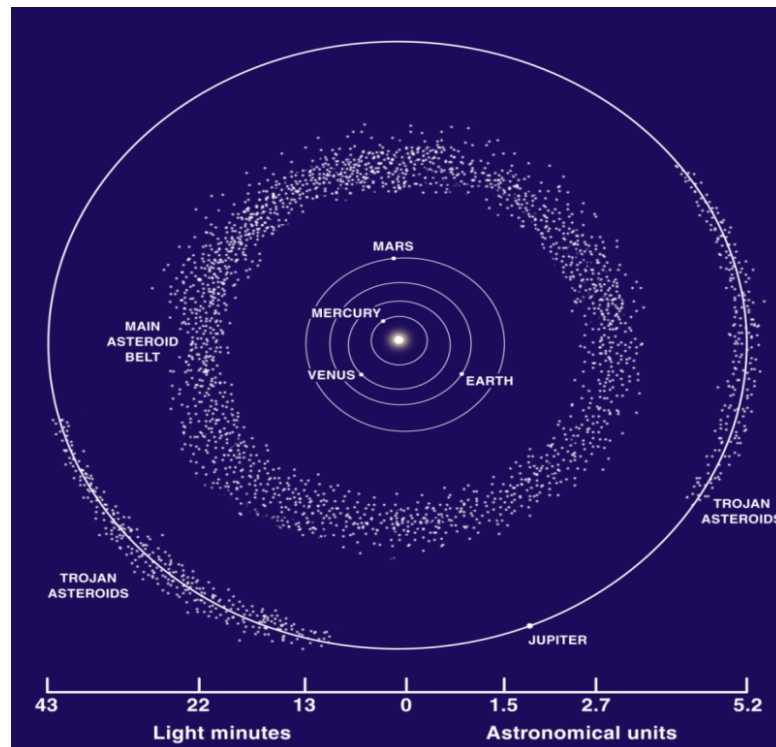


Figure 2.1 Location of the Main Asteroid Belt (Lunar and Planetary Institute)

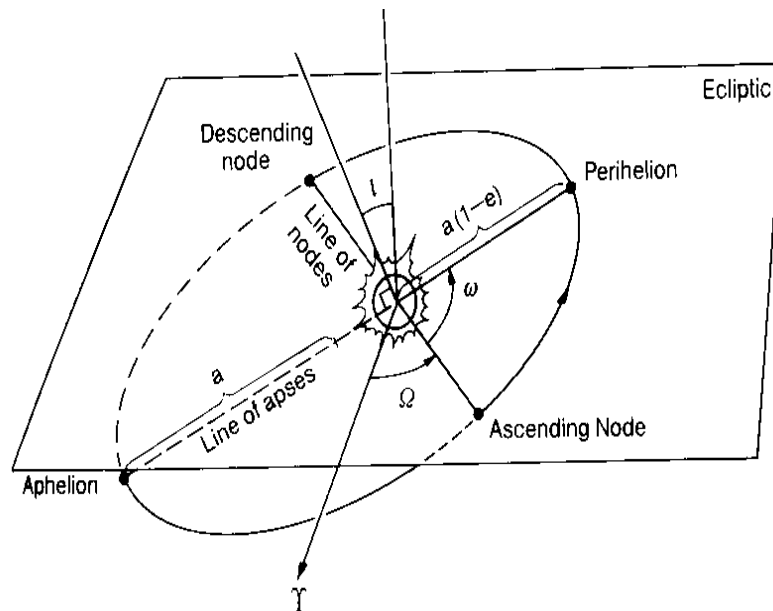


Figure 2.2 Orbital Parameters –Rieke, M. University of Arizona ([ircamera.as.arizona.edu/astro\\_250](http://ircamera.as.arizona.edu/astro_250))

An asteroid's orbit can be specified (Figure 2.2) by six parameters known as Keplerian elements:

$a$  – the semimajor axis, which is a measure of asteroid's average distance from the sun.

$e$  – the eccentricity, which describes the shape of the orbit.

$i$  – the inclination, which is measured relative to the plane of the ecliptic.

$\Omega$  – the longitude of the ascending node, which is the point where the orbit crosses the ecliptic plane moving north.

$\omega$  – the argument of perihelion, which is the angular distance along the orbit measured from the ascending node to the perihelion.

$v$  – the true anomaly, which is the angle between the direction of periapsis and the current position of the body

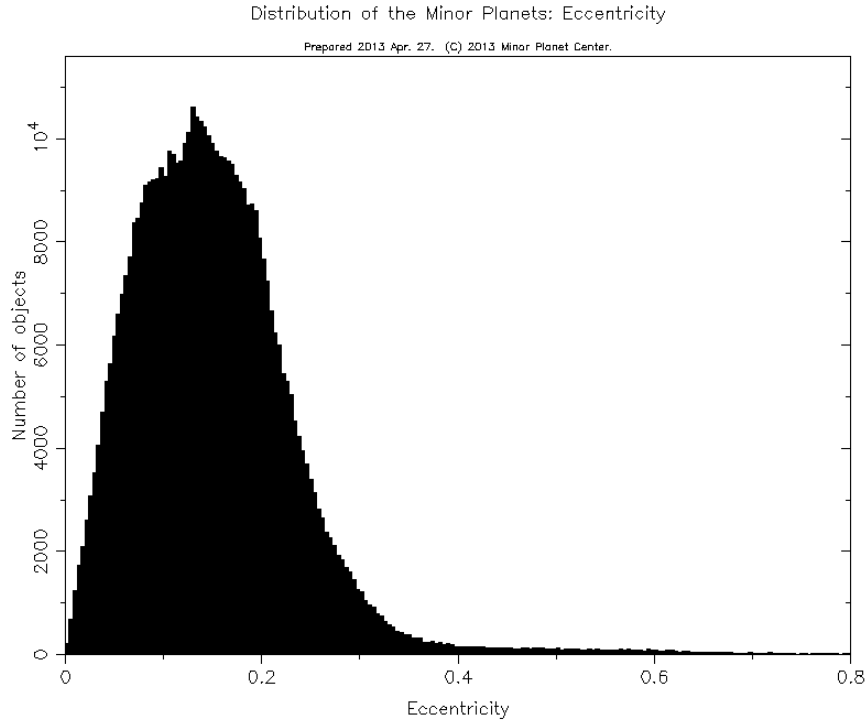


**Figure 2.3 Distribution of asteroid orbital eccentricities**

The majority of asteroids in the main belt are in moderately eccentric orbits (Figure 2.3) which follow a Rayleigh distribution:  $N(e) \propto \frac{e}{e_7} \exp\left(\frac{-e^2}{e_7^2}\right)$  where the mean eccentricity,  $e_7 \approx 0.14$  (De Pater, 2001). Their orbits tend to have a low inclination relative to the ecliptic plane; the majority of orbits have an inclination less than fifteen degrees (Figure 2.4) Statistically, most asteroids are expected to have experienced a violent collision on time-scales on the order of the age of the solar system (Öpik 1951). It is estimated that less than one percent of the original material still remains in the asteroid belt, the rest having been either destroyed by collision or ejected due to the effects of gravitational perturbations (Petit et al. 2001).



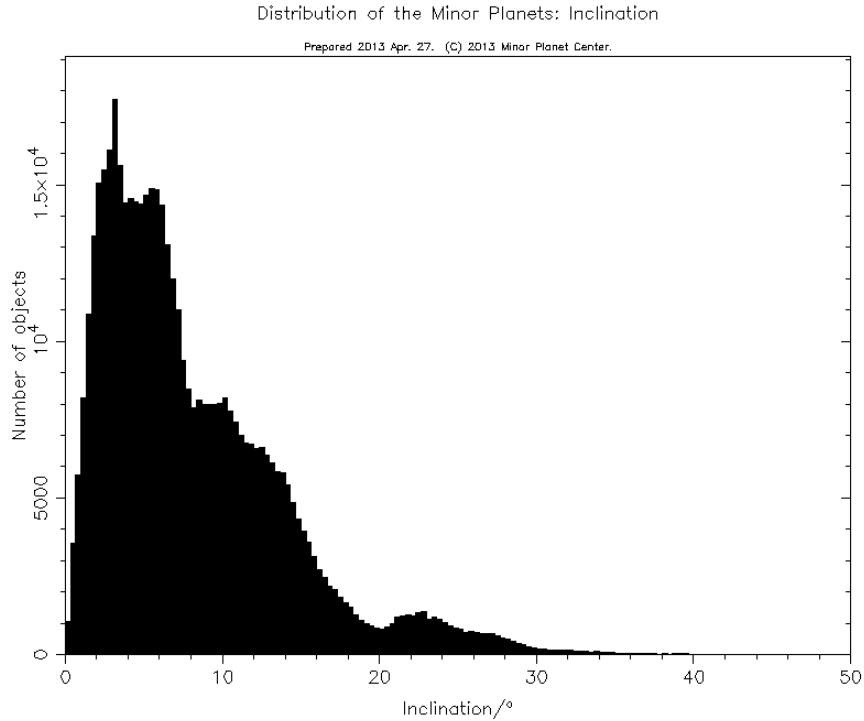


**Figure 2.4 Distribution of asteroid orbital inclinations (Minor Planet Center)**

A “Near Earth Asteroid” is defined by the International Astronomical Union as an asteroid in an orbit with a perihelion distance ( $q$ ) less than 1.3 AU (IAU). In order for a collision to move an asteroid from an orbit in the main belt into an Earth crossing orbit it would have to impart a  $\Delta V$  of roughly four kilometers per second. This pretty much rules out a simple billiard ball style collision mechanism, as an impact capable of imparting this much  $\Delta V$  would almost certainly destroy the asteroid in the process. Something a bit more subtle must be at work!

The distribution of asteroids in the main belt is non-uniform. Distinct gaps are apparent if one plots the number of asteroids as a function of their heliocentric distance (Figure 2.5). The presence of these gaps was explained by Professor Daniel Kirkwood who pointed out that two very prominent gaps exist at distances where an asteroid’s

orbital period corresponds to either  $1/3$  or  $1/2$  the orbital period of Jupiter. Kirkwood (1876) showed that these gaps were a manifestation of a resonance phenomenon known as orbital mean motion resonance. To visualize this phenomena consider an asteroid orbiting the Sun at a distance of 2.5 AU. The asteroid has an orbital period of 3.95 years which is one third the orbital period of Jupiter. It will complete three orbits around the Sun in the same time it takes Jupiter to complete one. This 3:1 resonance means that the asteroid and Jupiter will always be in conjunction at the same point in the asteroid's orbit and as a result the effects of Jupiter's gravitational perturbations on the asteroid's orbit accumulate over time. Eventually the asteroid is removed from the resonance either by a close flyby of a planet or impact with another planetary body. It has been discovered however that the Kirkwood gaps are being continuously replenished with asteroid fragments (Petit et al. 2001).

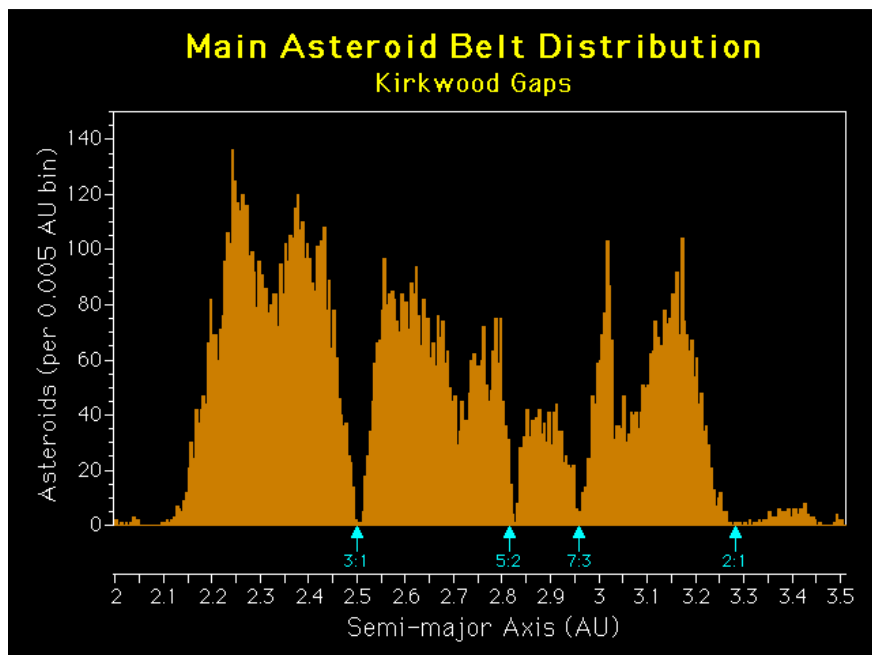


Figure 2.5 The Kirkwood Gaps (Institute For Astronomy, Hawaii)

The most prominent Kirkwood gaps correspond to the 4:1 resonance at  $\sim 2.06$  AU, the 3:1 resonance at  $\sim 2.5$  AU, the 5:2 resonance at  $\sim 2.82$  AU, the 7:3 resonance at  $\sim 2.95$  AU, and the 2:1 resonance at  $\sim 3.27$  AU. Additional, narrower gaps corresponding to weaker resonances also exist at 1.9 AU (the 9:2 resonance), 2.25 AU (7:2), 2.33 AU (10:3), 2.71 AU (8:3), 3.03 AU (9:4), 3.075 AU (11:5), 3.47 AU (11:6), and 3.7 AU (5:3).

Carl Gustav Witt's<sup>3</sup> discovery of 433 Eros established that a population of asteroids existed in orbits which intersect the orbits of the inner planets. At its January 18<sup>th</sup> 2012 perihelion 433 Eros came within 0.189 AU of the Earth (Figure 2.6). A satisfactory explanation for how an asteroid might migrate from the main belt into an Earth crossing orbit had to wait until the 1980's when computers had become sufficiently powerful to convincingly model asteroid orbital dynamics.

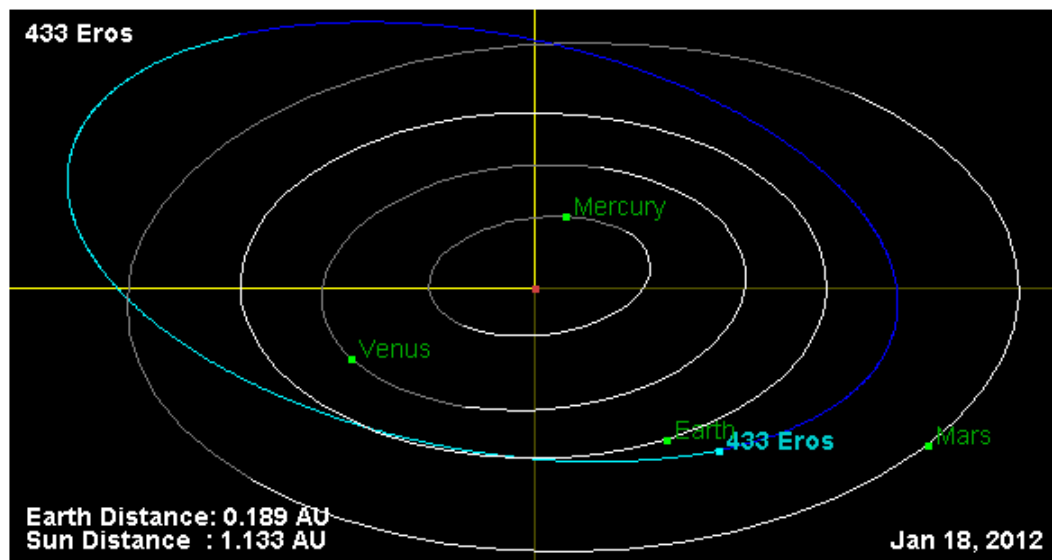


Figure 2.6 Orbit of 433 Eros (NASA JPL Small-Body Database Browser <http://ssd.jpl.nasa.gov/sbdb.cgi>)

<sup>3</sup> 433 Eros was independently discovered by Auguste Charlois at the Observatoire de Nice on August 13<sup>th</sup> 1898

Wisdom (1982) hypothesized that asteroids near the resonances could undergo sudden large jumps in eccentricity. His numerical simulations indicated that over periods of millions of years gravitational perturbations could force an asteroid into a highly eccentric orbit which may lead to either a collision or ejection from the belt. Wisdom (1983a) subsequently verified that this phenomenon was real. Using numerical integrations of the planar-elliptic restricted three-body problem he successfully reproduced these sudden increases in eccentricity. Wisdom commented that “large increases in eccentricity which were first seen with a mapping have now been seen in numerical integrations of the differential equations. This peculiar behavior is thus not an artifact of the mapping technique, but a phenomenon which real asteroids near the 3/1 commensurability might exhibit.”

Chirikov (1979), a pioneer in the study of dynamical chaos, proposed that every resonance phenomena should manifest a “chaotic zone”. Wisdom (1983a) in a systematic exploration of the evolution of sample asteroid trajectories discovered three basic classes of trajectories: chaotic trajectories, quasi-periodic trajectories inside the chaotic zone, and quasi-periodic trajectories outside the resonance region defined by the chaotic zone. He concluded that, within the age of the solar system, there was a fairly high probability that asteroids with chaotic trajectories would be removed from the main belt by collision or close encounter with the Sun, Mars, Jupiter, or Earth. This is now thought to be the mechanism responsible for clearing the Kirkwood gaps. Wisdom (1985a) further explored the origin of the Kirkwood gaps and demonstrated that the precise size and shape of the 3:1 gap could be explained by the removal of the chaotic and quasi-periodic planet crossing asteroids.

Another type of resonance known as a “secular” resonance can also modify an asteroid’s orbit sufficiently to remove it from the main belt. A secular resonance occurs when the rate of variation of either the longitude of perihelion or longitude of the ascending node ( $\Omega$ ) of an asteroid’s orbit becomes equal or very nearly equal to the rate of orbital precession of one of the major planets. The  $\nu_5$  resonance, for example, is due to a 1:1 commensurability between the frequency of rotation of the longitude of perihelion of an asteroid and the average frequency of rotation of Jupiter’s longitude of perihelion. The most important secular resonances as far as asteroids are concerned are the  $\nu_6$  resonance with Saturn, the  $\nu_5$  resonance with Jupiter, and the  $\nu_{16}$  resonance with both Saturn and Jupiter. Tisserand (1882) noted that the inner boundary of the main belt coincides with the location of the  $\nu_6$  resonance. Brouwer and van Woerkom (1950) calculated the frequencies of the main secular resonances in the solar system using a linear secular perturbation theory.

Williams (1969) developed a non-linear secular perturbation theory based on the Gauss averaging method which he used to study the long term evolution of asteroid orbits. He showed through numerical simulations (Williams, 1971) that the  $\nu_5$ ,  $\nu_6$  and  $\nu_{16}$  resonances have all produced gaps in the main belt. The region located around 2.05 AU, which is subject to the effects of both the  $\nu_6$  and  $\nu_{16}$  resonances and the 4:1 mean motion resonance, is strongly depleted (Figure 2.5). Williams (1973) suggested that the secular resonances might be an important mechanism for the delivery of asteroids and meteorites into near Earth orbits. His simulations showed that the orbits of fragments ejected from asteroids located near the secular resonances could, on time scales of around one million years, evolve to become Earth crossing. His calculations assumed that the fragments had

ejection velocities on the order of 300 meters per second. Such high velocities would imply that the resulting meteorites recovered on Earth should show evidence of having been shocked.

Williams and Faulkner (1981) collaborated to map the positions of the secular resonances in the asteroid belt (Figure 2.7). The  $\nu_6$  resonance surface traces a curve which delineates the upper bound of orbital inclination for the majority of asteroids in the main belt. The  $\nu_6$  and  $\nu_{16}$  secular resonances interact with the 4:1 mean motion resonance to define the inner edge of the main belt.

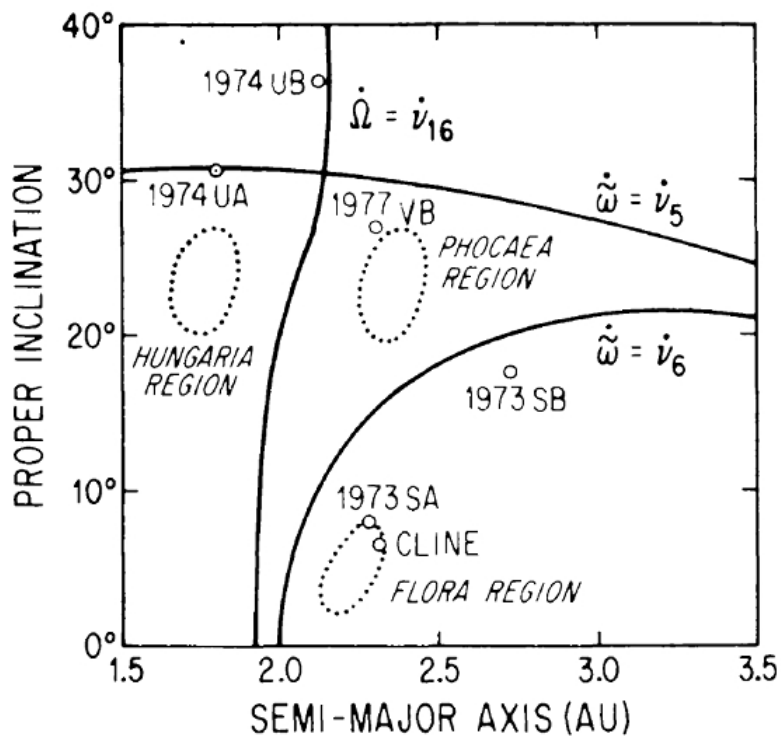


Figure 2.7 Location of the secular resonances in the asteroid belt (Williams & Faulkner 1981)

Froeschle and Scholl (1986) presented results of a numerical simulation of one million years of orbital evolution in the  $\nu_6$  secular resonance, which confirmed the location of the resonance predicted by Williams in 1969. They observed large increases

in eccentricity for all orbits originating in the resonance. The authors stressed that the increases in eccentricity were not due to the nearby 4:1 resonance as all of the test asteroids were located outside of this mean motion resonance. The most significant result from their simulation was that all test asteroids ended up in Earth crossing orbits.

Farinella et al. (1993) studied the NEA delivery process by modeling how asteroid fragments, ejected during crater formation on a parent body, enter the chaotic zones close to the 3:1 mean motion and  $\nu_6$  secular resonances. Their model considered 2355 main belt asteroids with semimajor axis less than 2.8 AU, eccentricity less than 0.3, inclination less than 30 degrees and a perihelion distance greater than 1.1 AU. This sampling methodology purposefully excluded high eccentricity/inclination and Earth approaching asteroids. Impacts were simulated as “isotropic ejection” events which produced a large number of fragments with random ejection velocity vectors. They determined that the efficiency of the NEA delivery process was dependent on a number of factors: (i) the mass vs. ejection velocity distribution of fragments, (ii) the escape velocity of the parent asteroid, (iii) the  $\Delta V$  required to reach a resonance, (iv) the width of the chaotic zones surrounding the resonance, and (v) the volume of material ejected per unit time.

Their results indicated that a large fraction of meteorites and NEAs could be generated by a small ( $\approx 1\%$ ) and possibly non-representative fraction of the known asteroid population, mostly made of relatively large bodies located in the neighborhood of the two resonances Farinella et al. (1993) Both resonances were found to be effective channels for fragment collection and delivery. The authors concede that their lack of understanding of how a significant fraction of fragments could be ejected at velocities of

hundreds of meters per second limited them to claiming only that their model seems internally consistent. One would expect meteorites ejected by such violent collisions to be significantly shocked, but this is not typically seen in the average meteorite.

Moons and Morbidelli (1995) went beyond the simple mathematical framework of the planar elliptic restricted three body problem and investigated secular motion in three dimensional space. This novel approach allowed them to study the role played by secular resonances *inside* mean motion resonances. Their main finding was that the two main secular resonances,  $\nu_5$  and  $\nu_6$ , do actually exist inside the mean motion resonances and that their interaction and overlap generates a wide layer of large scale chaos which they state is responsible for clearing the 7:3 Kirkwood gap.

Gladman et al. (1997) reported that their numerical simulations of test particles placed in orbital resonances in the main asteroid belt showed that the typical dynamical lifetimes of objects that could become near-Earth asteroids was only a few million years. The majority were destroyed by ending up in Jupiter-crossing orbits or by colliding with the Sun. Asteroids that were moved into near Earth orbits by the perturbing effects of resonances were still dynamically eliminated on time scales of around ten million years. The authors concluded that the implied short lifetimes for these asteroids may require a reassessment of our qualitative understanding of near-Earth asteroids and meteorite delivery mechanisms.

Dell'Oro and Cellino (2007) have developed a general statistical model to study the dynamical effects of non-destructive collisions on the long term evolution of orbits of small main belt asteroids with diameters less than 5 kilometers. The model analyses, in



general terms, how the efficiency of these dynamical effects is dependent upon the size distribution of the asteroid population, the physics of collisions, and the size and orbital parameters of the target. They have found that eccentricity and inclination are subject to a systematic decrease, whereas the semimajor axis can either increase or decrease depending on its initial value: the semimajor axis of asteroids located in the inner regions of the Main Belt tends to increase, whereas in the outer belt it tends to decrease. The boundary between the two different regimes is at semimajor axis values in the interval between 2.6 and 2.9 AU, for which the semimajor axis does not change in a systematic way.

Apart from collisions and resonance perturbations there exists a third type of phenomena that can modify asteroid orbits. The Yarkovsky and YORP effects are thermal radiation effects that can alter the semimajor axis and spin vectors of asteroids with diameters less than 20 km. The Yarkovsky effect is capable of moving asteroids from the main belt into chaotic resonance zones which can ultimately transport them into Earth-crossing orbits. Farinella and Vokrouhlický (1999) theorized that many of the main-belt resonances are being continually replenished with small, sub-20 kilometer diameter asteroids by the Yarkovsky effect.

The Yarkovsky effect is named in honor of Russian engineer Ivan Osipovich Yarkovsky who proposed circa 1900 that the diurnal heating of a rotating asteroid should cause it to experience a force, which over time, would be capable of modifying its orbit. The basic concept is that incident sunlight heats the surface of the asteroid and as this heat is radiated away to space, in the form of thermal infrared radiation, the IR photons

impart a tiny force<sup>4</sup>. Asteroids have thermal inertia so it takes a finite time to dissipate this energy. Since the asteroid is rotating, away from the sub-solar point, the IR photons are radiated from the “afternoon” side of the asteroid. The recoil effect from this anisotropic emission of thermal radiation (illustrated by the wide arrows in Figure 2.8a) causes an asteroid to slowly spiral outward from the Sun over a time scale of millions of years. An asteroid with retrograde rotation would spiral inward. The magnitude of this perturbation is a function of the asteroid's mass, surface thermal characteristics, and heliocentric distance. There is also a seasonal Yarkovsky effect (Figure 2.8b), which results from the temperature differences between the spring/summer and autumn/winter hemispheres of an asteroid. Numerical simulations have shown that the eccentricities of main belt asteroids are only indirectly affected by the Yarkovsky effect. Orbital inclination is not expected to undergo significant alteration due to the Yarkovsky effect (Bottke et al., 2000; Spitale and Greenberg, 2002).

---

<sup>4</sup> The photon carries away momentum  $p = E/c$ , (where  $p$  = momentum,  $E$  = energy,  $c$  = speed of light) and in doing so imparts a kick to the asteroid due to the conservation of momentum.

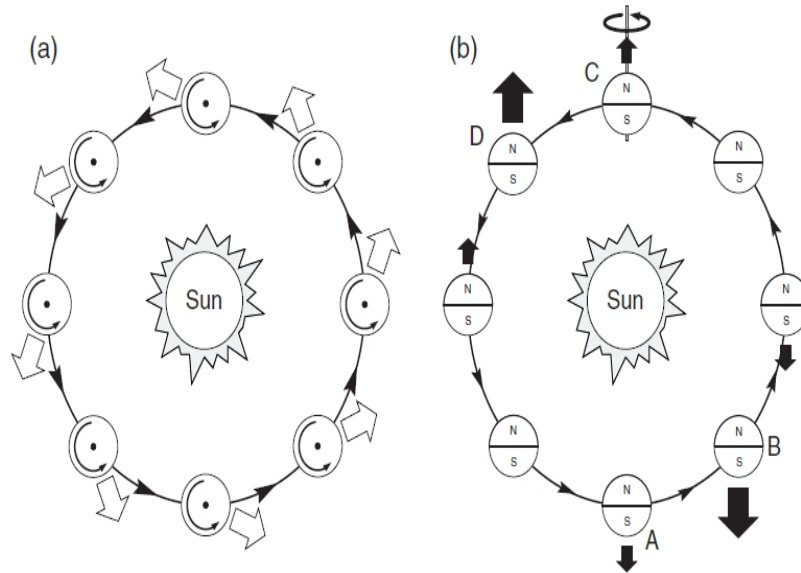


Figure 2.8 (a) The diurnal Yarkovsky effect. The asteroid's spin axis is perpendicular to the orbital plane (b) The seasonal Yarkovsky effect, with the asteroid's spin axis in the orbital plane. (Bottke 2002)

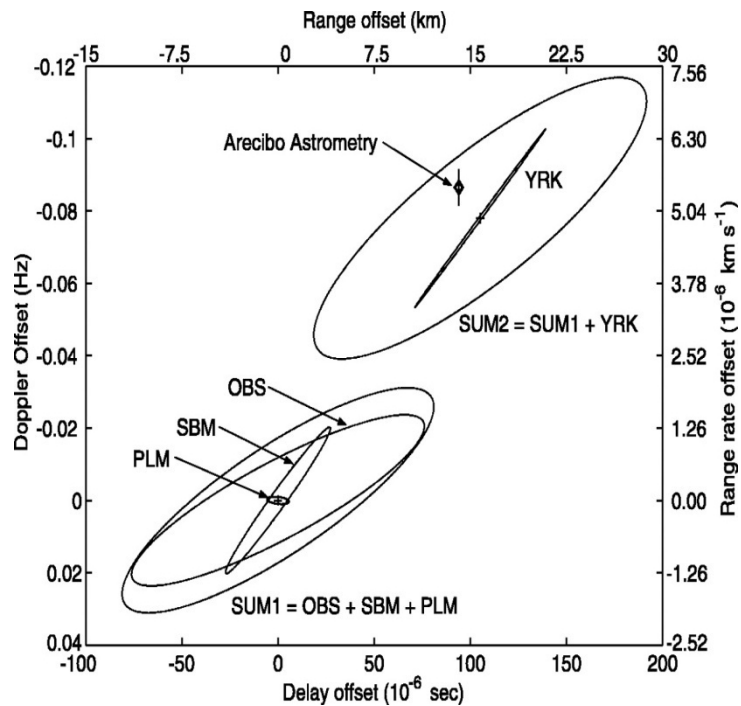
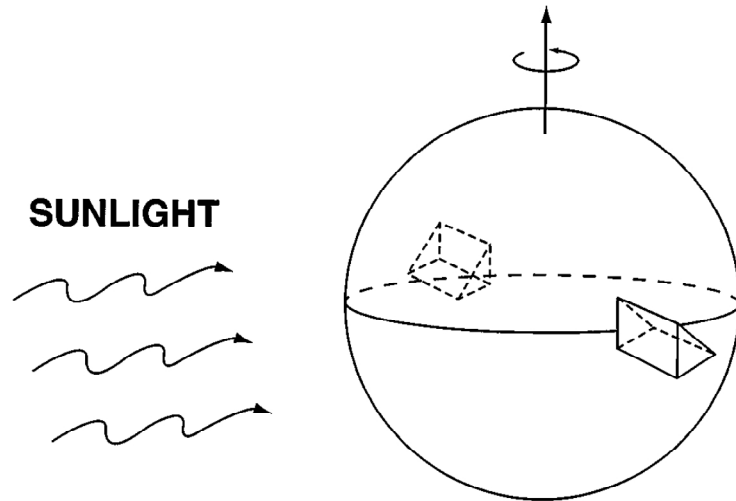


Figure 2.9 Detection of the Yarkovsky effect on near-Earth asteroid 6489 Golevka. (Chesley et al 2003).

Chesley et al. (2003) reported the first direct detection of the Yarkovsky effect on a near-Earth asteroid (6489 Golevka). Their discovery was based on comparison of radar ranging from the Arecibo telescope with astrometric measurements made over the preceding decade. Figure 2.9 above shows the results. The Ellipses labeled OBS, SBM, PLM, and YRK represent the dispersions caused by uncertainties in astrometric measurements, small body masses, planetary masses, and Yarkovsky modeling, respectively. The SUM1 ellipse, which is the combination of the OBS, SBM, and PLM uncertainties, depicts the 90% confidence region for a non-Yarkovsky prediction. Similarly, the SUM2 ellipse, which includes the added uncertainty of the Yarkovsky modeling, represents the 90% confidence region for the prediction with Yarkovsky accelerations. The actual Arecibo radar delay and derived Doppler measurement at this epoch is shown by a diamond with error bar Chesley et al (2003)

The term “YORP” effect, short for “Yarkovsky–O’Keefe–Radzievskii–Paddack”, was coined by Rubincam (2000). These four researchers laid the ground work in the study of the effects of anisotropic thermal radiation on small irregular bodies. The YORP effect is capable of moving objects into resonances by spinning up a body to the point where it disintegrates and throws out pieces that could reach a nearby resonance. The physics underlying the YORP effect is essentially the same as the Yarkovsky effect with one major distinction; it is only significant if the asteroid has an irregular shape. Figure 2.10 from Rubincam (2000).shows a simplified model of the effect. The asteroid is modeled as a sphere with two wedges attached to its equator. The asteroid is modeled as a blackbody , so that it absorbs all the sunlight falling upon it. The solar energy is reemitted as thermal radiation, which causes a net torque on the asteroid



**Figure 2.10 YORP induced spin-up of an asymmetrical asteroid. (Rubincam 2000)**

Farinella et al. (1998) gives the following formula for the timescale of YORP induced rotation rate:  $t_{rot} \approx 3.34 \times 10^6 \text{ years} \left(\frac{R}{1m}\right)^{\frac{1}{2}}$  where R is the asteroid's radius in meters. For smaller objects the YORP effect becomes dominant over collisions due to the  $R^2$  dependence of the YORP timescale as compared to the  $R^{\frac{1}{2}}$  dependence assumed for collisions. Rubincam (2000) states that "YORP can be expected to completely dominate collisions in the inner Solar System for  $R < 5\text{-km}$  asteroids due to their small size, increased insolation, and smaller population of impactors compared to the main belt". He found that the YORP effect may spin up or spin down 5-km-radius asteroids on a  $10^8$  year timescale. Smaller asteroids were found to spin up even faster due to the radius-squared dependence of the YORP timescale. The limiting factor on the effectiveness of YORP in the inner solar system may be the fact that NEAs have half-lives of about 10 million years before they impact a planet or the Sun, or are ejected from the solar system by Jupiter (Gladman et al., 1997)

Lowry et al. (2007) reported the first direct detection of the YORP effect in an asteroid based on precise optical photometric observations of a small near-Earth asteroid, 2000 PH5, acquired over 4 years. They found that the asteroid has been continuously increasing its rotation rate,  $\omega$ , over this period by  $d\omega/dt = 2.0 (\pm 0.2) \times 10^{-4}$  degrees per day. Taylor and Margot (2007) mapped the shape and located the spin pole of 2000 PH5 between 2001 and 2005 using the Arecibo Observatory in Puerto Rico and NASA's Goldstone telescope in California. The observed spin-rate was seen to change from year to year (black dots). The solid curve is the expected theoretical YORP strength derived from the 3-D shape model. Their calculation of the YORP acceleration is in excellent agreement with results obtained by Lowry et al. (2007) (Figure 2.11)

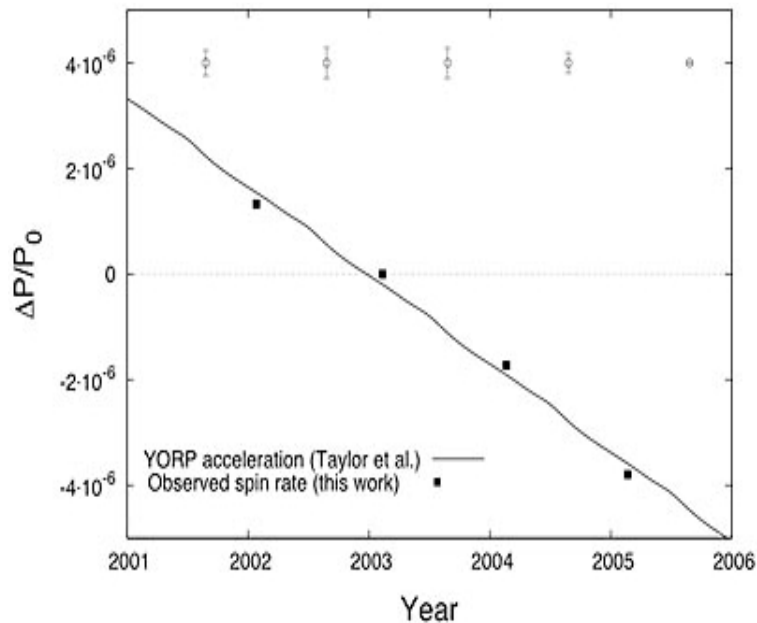


**Figure 2.11 Direct detection of the YORP effect in near-Earth asteroid, 2000 PH5 (Lowry et al., 2007).**

## Chapter III

### Mineralogical Analysis of Asteroid Surfaces

The earliest theory regarding the mineralogical composition of asteroids seems to have been proposed by F.G. Watson in his book entitled "*Between the Planets*" published in 1941. Noting that the color of a material is often related to its chemical composition, Watson suggested that "Through the study of colors of asteroids we hope to determine what terrestrial materials they resemble and whether they treat light in the same manner as meteorites..." Hardersen (2003) points out that applying a color index (a method that is commonly used to classify stars by their surface temperature) to asteroid classification is meaningless as the mechanism by which stars radiate light is completely different. A star's color (peak emission wavelength) is defined by its blackbody temperature whereas an asteroid, which does not have any internal heat source, merely reflects incident solar light. Watson's efforts to classify asteroids based on their color and implied mineralogy were ultimately futile. Chapman (1971), in his review of spectro-photometric studies of asteroids, comments that "there are far too many minerals for a one-dimensional characterization of asteroid color (or color index) to suggest even a compositional class, let alone a specific composition. But when the full spectral reflectivity curve is well defined, for instance in the 24 narrow band interference filters we have been using, the measurements are considerably more diagnostic". Burns (1970, 1993) applied Crystal Field Theory (CFT) to explain the spectral absorption features observed in rock forming minerals containing transition metal ions, especially  $\text{Fe}^{2+}$ .

## 1. Overview of Crystal Field Theory

Crystal Field Theory (CFT) is a chemical bonding model developed by Hans Bethe, which describes the interaction between the metal cation and surrounding ligands in a transition metal coordination complex. In 1929 Henri Becquerel proposed that the metal cation in a complex ionic crystal was subject to an electric field originating from the surrounding ligands. Bethe (1929) formalized Becquerel's proposal and applied group theory and quantum mechanics to existing electrostatic theory in a seminal paper that investigated how the symmetry and strength of a crystalline field affects the electronic levels of the metal ions. Van Vleck (1932) pioneered the application of this new theory to chemistry and made further refinements throughout the 1930s.

Crystal Field Theory is based on a number of assumptions:

1. Ligands are considered to be negative point charges situated on a lattice surrounding the metal cation.
2. The interaction between the metal cation and the ligands is assumed to be purely electrostatic.
3. The electrons in the cation are subject to a repulsive electrostatic field emanating from the electrons in the surrounding ligands.
4. As a result of this repulsive electrostatic field the electrons in a transition metal cation occupy the d-orbitals which permit the largest physical separation from the ligands.



5. Negatively charged ligands result in ion-ion interaction and neutral ligands produce ion-dipole interaction.

A transition metal, as defined by The International Union of Pure and Applied Chemistry (IUPAC), is "an element whose atom has an incomplete d sub-shell, or which can give rise to cations with an incomplete d sub-shell". The chemistry of the transition metal group<sup>5</sup> is determined by these incomplete d subshells. Each of the five 3d subshells, designated as  $d_{yz}$ ,  $d_{xy}$ ,  $d_{xz}$ ,  $d_z^2$  and  $d_{x^2-y^2}$  (Figure 3.1) can hold two electrons. The shapes of the lobes in Figure 3.1 represent probability density functions for the instantaneous location of these electrons.

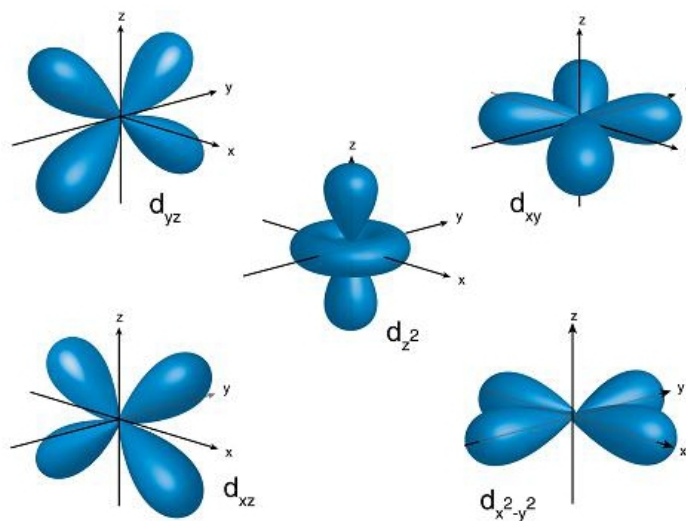


**Figure 3.1 Shape of the d sub shells. (USGS)**

If the metal cation is a gaseous ion (not chemically bonded) then the d sub shells all have equal energy (Figure 3.2). This state is known as “degeneracy”. When the cation is inside a crystal lattice its 3d electrons experience differing degrees of electrostatic repulsion

---

<sup>5</sup> The elements of the first transition series are: Sc, Ti, V, Cr, Mn, Fe, Co, Ni, Cu and Zn. Iron is the most cosmically abundant of these.

based on the orientation of their sub shell with respect to the surrounding ligands. In octahedral coordination, such as in a silicate mineral, the metal cation is surrounded by six ligands. The lobes of the  $d_z^2$  and  $d_{x^2-y^2}$  sub shells are pointed towards the ligands, thus they experience a stronger electrostatic repulsion than the  $d_{yz}$ ,  $d_{xy}$ ,  $d_{xz}$  sub shells whose lobes point between the ligands. This difference in the strength of repulsion causes a splitting of the d sub shells into two discrete energy levels,  $t_{2g}$  and  $e_g$  (where  $t$  signifies a threefold degeneracy and  $e$  a twofold degeneracy). The  $g$  subscript refers to the fact that the sign of the electron's wave function does not change on inversion.

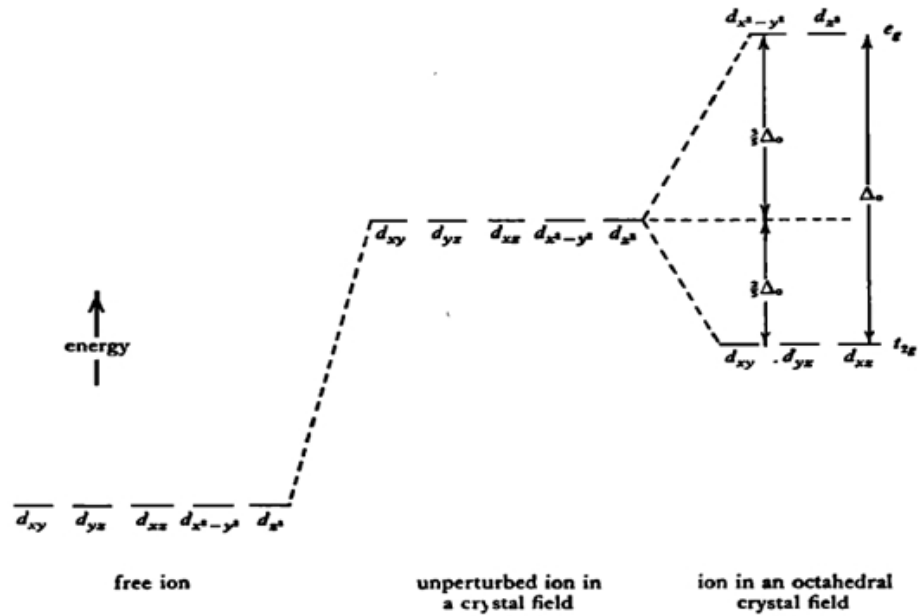
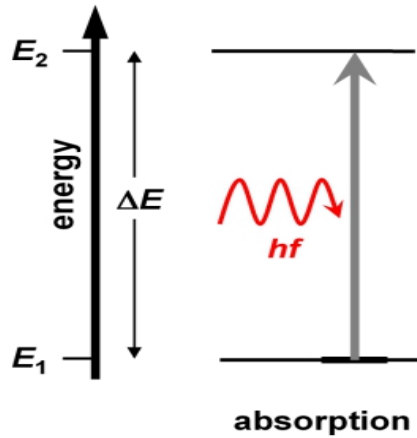


Figure 3.2 Relative energy levels of the d sub shells of a transition metal as a free ion, as an unperturbed ion in a crystal field and split due to an octahedral crystal field (Burns 1970).

The energy difference between the  $t_{2g}$  and  $e_g$  levels is known as the “crystal field splitting parameter” or  $\Delta_0$ . When photons, with energies equal to  $\Delta_0$ , interact with

electrons in the  $t_{2g}$  sub shell (Figure 3.2) they are absorbed and excite the electrons to the higher energy  $e_g$  level.



**Figure 3.3 Interaction between a photon of energy  $E = hf$  and an electron in a mineral crystal.  $\Delta E$  is the difference in energy between sub shells,  $h$  is Planck's constant ( $6.626068 \times 10^{-34} \text{ m}^2 \text{ kg s}^{-1}$ ) and  $f$  is the frequency of the photon.**

The probability of these energy level transitions are governed by selection rules. The Laporte or parity selection rule states that transitions can occur only between states that differ in parity; that is, one state must have a symmetric (g) wave function and the other an antisymmetric (u) wave function (Burns, 1993). Thus, accord to the Laporte selection rule, an electron transfer between the  $t_{2g}$  and  $e_g$  energy levels should be impossible. However, the rule can be relaxed by three factors: first, by the absence of a centre of symmetry in the coordination polyhedron<sup>6</sup>; second, by mixing of d and p orbitals which possess opposite parities; and third, by the interaction of electronic 3d orbital states with odd-parity vibrational modes. Burns (1993) states “since transitions between d and p orbitals are allowed, a mechanism is available for the normally Laporte-

---

<sup>6</sup> Real world minerals have imperfect crystal structures

forbidden transitions of an electron between e-type and  $t_2$ -type 3d orbital in a tetrahedrally coordinated transition metal ion. This leads to an absorption band in a spectrum, the intensity of which is proportional to the extent of mixing of the d and p orbitals. The spin-multiplicity rule states that the total number of unpaired electrons in an atom must remain unchanged during an electronic transition. Spin allowed transitions are distinguished in intensity from very weak spin-forbidden transitions (Burns, 1993).

The interaction between an incident photon of energy  $\Delta_0$  and the mineral crystal creates an absorption feature in the spectrum of reflected light. The mean wavelength of the feature is determined the crystal field splitting parameter. There are many variables that determine the crystal field splitting parameter such as the size of the metal cation, the symmetry of the ligands in the crystal lattice structure, their inter atomic distances, etc. Suffice it to say that each naturally occurring mineral has a unique crystalline and electronic structure which, provided it contains a transitional metal cation, will produce spectral absorption features that are unique to that particular mineral.. We can use our understanding of these diagnostic spectral features to constrain the mineralogy of an asteroid surface.

The instantaneous width of an absorption feature is determined by variations in the crystal field splitting energy resulting from thermal vibrations of the cation and anion position combined with the slope of the CF energy levels. The envelope of the instantaneous splitting energies forms a Gaussian distribution, which determines the shape and width of the individual absorption features (Burns, 1993).

## 2. Overview of Spectroscopic characterization of asteroid mineralogy

McCord et al. (1970) were the first to measure the reflectance spectra of an asteroid at visible and near infrared wavelengths. Their target was the bright asteroid 4 Vesta. The spectrum was taken using a set of narrow band interference filters with centers between 0.3 and 1.1 microns.

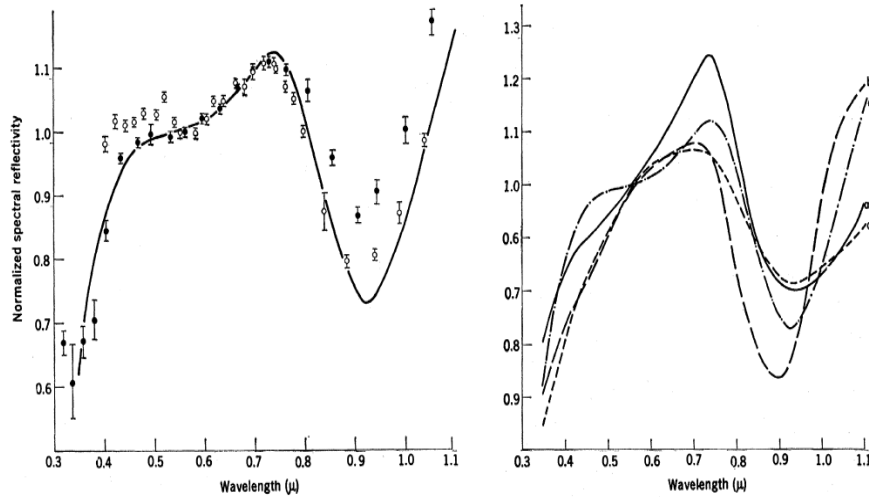


Figure 3.4 Reflectance spectra of asteroid 4 Vesta compared with a lunar sample and various meteorites. (McCord et al 1970)

The authors reported that the reflection spectrum for Vesta contained “a strong absorption band centered near 0.9 microns and a weaker absorption feature between 0.5 and 0.6 microns”. They also observed that the reflectivity decreased strongly in the ultraviolet. The authors noted that the reflection spectrum for asteroids Pallas and Ceres did not contain the 0.9-micron feature. Their interpretation was that the strong 0.9-micron feature seen in the spectrum was possibly the result of electronic absorptions in ferrous iron on the M2 site of a magnesian pyroxene similar to that seen in certain

basaltic achondrites. They supported their conclusion by comparing Vesta's reflectance spectrum with laboratory spectral measurements of meteorites and Apollo 11 lunar samples (Figure 3.4). Left – Telescopic spectra of Vesta (points) compared to laboratory reflectance of the Nuevo Laredo meteorite. Right: (a) Lunar sample returned by Apollo 11 (b) bronzite (orthopyroxene) (c) Holbrook chondrite (d) basaltic achondrite, Nuevo Laredo The 0.9 micron absorption feature is known to occur in Mg-rich orthopyroxene or pigeonite and is produced by the  $\text{Fe}^{2+}$  cation in six fold coordination (Bancroft and Burns, 1967).

According to Adams (1970) pyroxenes appear to be the most important group of minerals for the purpose of interpreting the spectra of rock and rock-derived surfaces in the solar system. Pyroxene is composed of single chains of silica tetrahedral, which form either monoclinic or orthorhombic crystals (Figure 3.5). The purple spheres in the crystal structure represent magnesium in the M1 sites and the yellow spheres are calcium in the M2 sites.  $\text{SiO}_4$  tetrahedra (red = O & blue = Si) are shown on the right of the image. The chain structure can incorporate a variety of cations.

The general formula for a pyroxene is  $\text{X,Y}(\text{Si, Al})_2\text{O}_6$  where X and Y represent metal cations. X, which occupies the M2 cation site, can be either: Ca, Na,  $\text{Fe}^{2+}$ , Mn, Mg, or Li. Y, which occupies the M1 site, can be either: Mg,  $\text{Fe}^{2+}$ , Mn, Ni, Al,  $\text{Fe}^{3+}$ , Cr, Ti or V (Burns, 1993). The M1 cation sites are physically smaller than the M2 sites, since they are at the apices of the tetrahedral chains. Substitutions by other cations, such as Li and Zr, does not result in distinct absorption bands (Cloutis 2002).

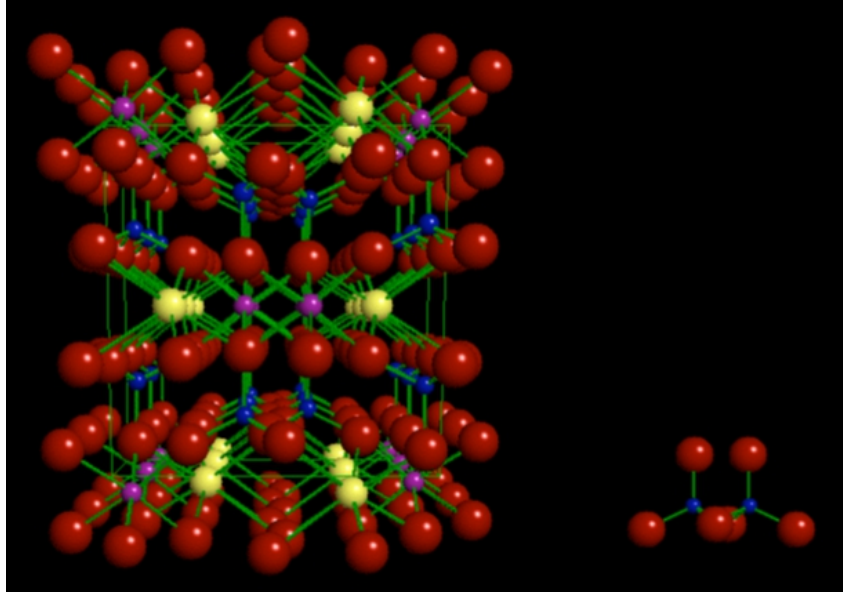


**Figure 3.5 Crystal structure of Diopside, a monoclinic pyroxene mineral. (USGS)**

Absorption bands, centered near 1  $\mu\text{m}$  and/or 2  $\mu\text{m}$ , occur in the near-infrared reflectance spectra of pyroxenes. The wavelength of these bands vary as functions of pyroxene composition, specifically as a function of  $\text{Fe}^{2+}$  concentration, making possible mineralogical and chemical deductions based on spectral reflectance curves (Adams, 1974).  $\text{Fe}^{2+}$  ions in the highly distorted, non-centrosymmetric, M2 site are responsible for the positions and intensities of the 1  $\mu\text{m}$  and 2  $\mu\text{m}$  absorption bands. The 1  $\mu\text{m}$  absorption feature is the result of electronic transitions from the ground to the highest energy excited state and the 2  $\mu\text{m}$  feature is produced by electrons transition to the next lower energy excited state (Figure 3.6 below). The observed transitions in the spectra are from (a) the M1 site and (b) M2 site.

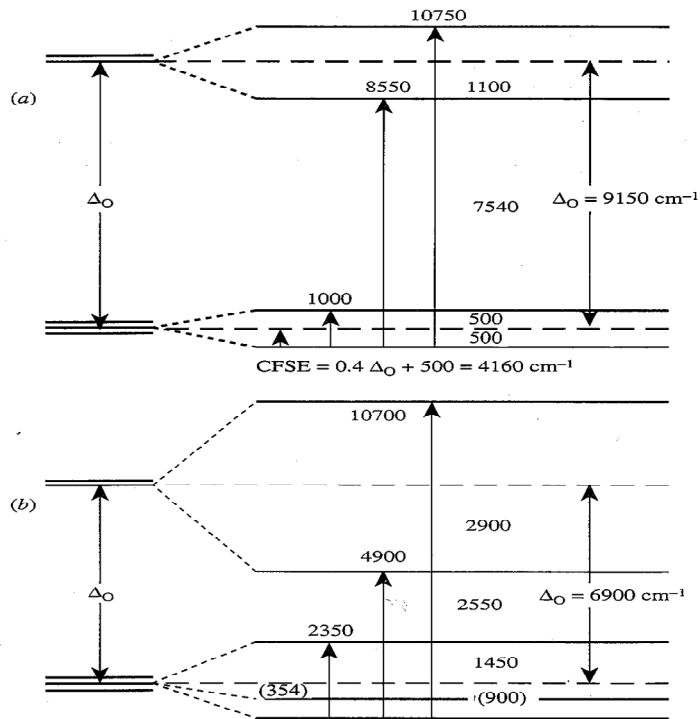


Figure 3.6 3d orbital energy level diagrams for  $\text{Fe}^{2+}$  ions in orthoferrosilite. (Burns, 1985a).

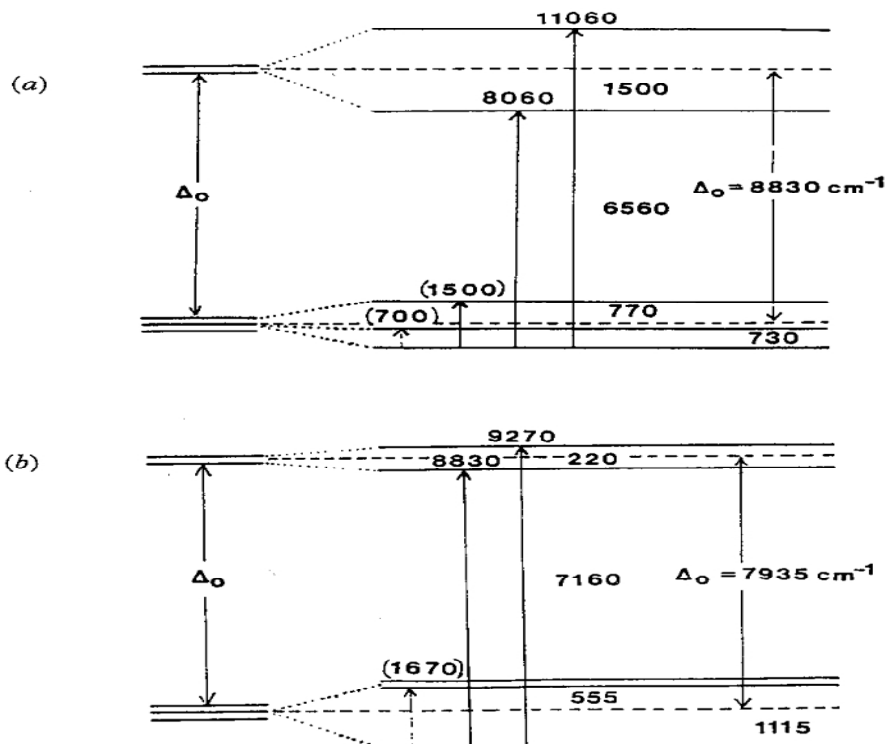


Figure 3.7 3d orbital energy level diagram for  $\text{Fe}^{2+}$  ion in fayalite. (Burns, 1985a).



Olivine is a magnesium iron silicate with the general formula  $(\text{Mg,Fe})_2\text{SiO}_4$ . Olivine has a single broad absorption feature at approximately 1 micron. Which is due to three narrower overlapping features: a central feature at  $\sim 1.04 \mu\text{m}$  and two side lobes at  $\sim 0.8$  and  $1.3 \mu\text{m}$ . The precise wavelength varies as a function of the relative abundance of the  $\text{Fe}^{2+}$  and  $\text{Mg}^{2+}$  cations. Figure 3.7 illustrates the 3d orbital energy level diagram for the  $\text{Fe}^{2+}$  ion in fayalite, which is the iron rich end member of the olivine solid solution series.

### **A Short History of Asteroid Taxonomy**

A number of asteroid classification schemes have been proposed over the years. The first extensive asteroid taxonomy was based on narrowband spectrophotometric measurements of 98 asteroids made by Chapman et al. (1971). He described two distinct groups of objects based on their reflectance properties. Zellner et al. (1973), recognizing a distinct bimodal distribution in albedos, suggested asteroids could be divided into two groups: dark “carbonaceous” types and brighter “stony” types. Chapman et al. (1975) surveyed 110 asteroids using a combination of visible and near-IR narrowband spectrophotometry with polarimetric and radiometric albedo measurements, which they used to classify asteroids into a taxonomy based on observational parameters. The authors proposed a bimodal C, S taxonomy having concluded that “more than 90% of the asteroids are shown to fall into two broad groups (C and S) which are compositionally similar to carbonaceous and stony meteorites, respectively”. Unfortunately, their decision to name the taxonomic classes in a way that implies a compositional relationship has led to confusion because it fails to recognize that significant compositional diversity may exist within each class.

A second classification system based on a much larger observational dataset of 523 asteroids was introduced by Bowell et al. (1978). The classifications were entirely empirical and independent of any specific mineralogical interpretation. Instead, Bowell et al. (1978) chose to base the system on seven directly observable parameters obtained from polarimetry, radiometry, spectrophotometry, and UVB photometry. They list the advantages of the classification system as: (1) wide application, since it depends upon a few readily observable parameters; (2) clear distinction between the major albedo classes; (3) it permits ready identification of unusual objects from reconnaissance data; and (4) it probably distinguishes objects that are geochemically differentiated from those with more primitive surface compositions. The system added three new classes M, E and R (metals, enstatites<sup>7</sup> and reds) and a fourth “unclassifiable” designation to Chapman et al.’s (1975) bimodal taxonomy. M-type asteroids were considered to resemble nickel-iron meteorites. The E-types are characterized by an albedo greater than 0.23 and the R-type asteroids have a similar albedo to the enstatite type but their spectra are much redder. “Of the 523 asteroids classified, 190 are identified as C objects, 141 as S type, 13 as type M, 3 as type E, 3 as type R, 55 as unclassifiable, and 118 as ambiguous” (Bowell et al 1978).

Gradie & Tedesco (1982) reported that it appeared, based on a variety of observations, mainly albedos derived from radiometry and eight-filter broadband spectrophotometry, that the asteroid belt is highly structured and composed of at least six major compositionally distinct regions. The authors state that *if* the observed differences among the asteroid types are truly compositional in nature, then the type distributions can

---

<sup>7</sup> Enstatite, from the Greek “*enstates*” or “adversary” in reference to its resistance to melting, is common in mafic igneous rocks and is the magnesium end member of the pyroxene silicate mineral series (MgSiO<sub>3</sub>)

be interpreted as representing gross compositional changes across the belt... The authors believe that the inferred composition of the asteroids in each semimajor axis region is consistent with the theory that the asteroids accreted from the solar nebula at or near their present location. They concluded that the general evolution of predominant compositional type from S to C to D with increasing heliocentric distance is evident, as is the spectral homogeneity of the Eos, Koronis, Nysa, and Themis families.

Tholen (1984) expanded on the earlier classification schemes, combining radiometric albedo measurements with spectrophotometric data from the Eight Color Asteroid Survey (ECAS) (Zellner et al. 1985). The survey used a dual channel photometer to conduct reflection spectrophotometry of 589 minor planets using a photometric system which consisted of eight filter passbands ranging from 0.34- to 1.04- $\mu\text{m}$ . Tholen (1984) classified asteroids into 14 groups based on their spectral parameters plus albedo. Earlier work by Gradie and Tedesco (1982) had discerned a systematic change in asteroid composition with increasing heliocentric distance which Tholen's taxonomy system subsequently confirmed.

Bell et al. (1988) conducted the first near infrared survey of the main asteroid belt, covering 0.8 to 2.5  $\mu\text{m}$ . The "52-color survey" observed over 100 objects and focused mainly on S-type asteroids all of which had estimated diameters greater than 20 km. Probably the most notable finding reported from the survey was that: "The taxonomic types can be grouped into "superclasses corresponding to the classic igneous, metamorphic and sedimentary rock types" (Bell et al., 1988). Bell et al. (1988) goes on to posit the idea that a central metamorphic heating mechanism, which declined very rapidly with increasing heliocentric distance, produced these radially distinct zones.

TABLE 1:  
RELATIONSHIP OF ASTEROID AND METEORITE CLASSIFICATION SYSTEMS

| Bell<br>Superclass | Tholen<br>Class | Inferred<br>Minerals | Meteorites                    |
|--------------------|-----------------|----------------------|-------------------------------|
| PRIMITIVE          | D               | Clays, Organics      | (None)                        |
|                    | P               | Clays, Organics      | (None)                        |
|                    | C               | Clays, C, Organics   | CI and CM chondrites          |
|                    | (Eos)           | Ol, Pyx, Carbon      | CV and CO chondrites          |
| METAMORPHIC        | T               | ?                    | ?                             |
|                    | B+G+F           | Clays, Opaques       | Altered C. C.s                |
|                    | Q               | Pyx, Ol, Grey NiFe   | H, L, LL Chondrites           |
| IGNEOUS            | V               | Plag, Pyx, Ol        | Basaltic Achondrites          |
|                    | R               | Ol, Pyx              | Ol-rich achondrites?          |
|                    | S               | Pyx, Ol, Red NiFe    | Pallasites, Lodranites, Irons |
|                    | A               | Ol                   | Brachinites                   |
|                    | M               | NiFe                 | Irons                         |
|                    | E               | Fe-free Pyx          | Aubrites                      |
|                    |                 | (Mars)               |                               |
|                    | (Moon)          |                      | (Lunar meteorites)            |

**Table 1 from Bell et al. (1988). The 52-Color Asteroid Survey: Final Results and Interpretation.**

Tedesco et al. (1989) combined broadband U, V and  $x$  ( $\lambda_{\text{eff}} = 0.36, 0.55$  and  $0.85 \mu\text{m}$ ) photometry with *IRAS*<sup>8</sup> albedos to define a three parameter asteroid taxonomy. These parameters, ( $U-V$ ,  $v-x$  color indices and visual geometric albedo) were used to create a classification system which placed 96% of the 357 sampled asteroids into 11 taxonomic classes. 10 of the 11 classes were analogous with classes previously defined in earlier taxonomic schemes. Of the 14 asteroids that did not fit into a classification 3 (2 Pallas, 4 Vesta and 349 Dembowska) were already known to have unique surface compositions.

---

<sup>8</sup> The Infrared Astronomical Satellite, launched in 1983, mapped 96 % of the sky at 12, 25, 60 and 100  $\mu\text{m}$ .

The remaining asteroids were considered to have either unique compositions or to have been misclassified due to poor observational data.

Bus and Binzel (2002) proposed a “feature based” taxonomy using data on 1447 asteroids (106 near-Earth asteroids) observed during the 2<sup>nd</sup> Small Main-belt Asteroid Spectrographic Survey (SMASS). Their classification system is based on 26 different color curves and seeks to refine Tholen’s C-S-X taxonomy. The SMASS was a visible wavelength survey covering 0.44- $\mu\text{m}$  to 0.92- $\mu\text{m}$  conducted by MIT in the early 1990s at Kitt Peak National Observatory (Xu et al. 1995). When one considers the limited wavelength coverage of SMASS it is clear that mineralogical interpretations of the spectra are difficult if not impossible.

The main problem with asteroid taxonomic schemes is that the asteroid’s classification is generally not well correlated with its actual mineral composition. That objects with different taxonomic classifications are composed of different materials seems fairly certain but what is not so clear is that asteroids with the same classification are necessarily composed of similar material. Gaffey et al. (1993) demonstrated that significant mineralogical diversity exists within the S taxonomic class which includes both differentiated and primitive members (Figure 3.8 below).

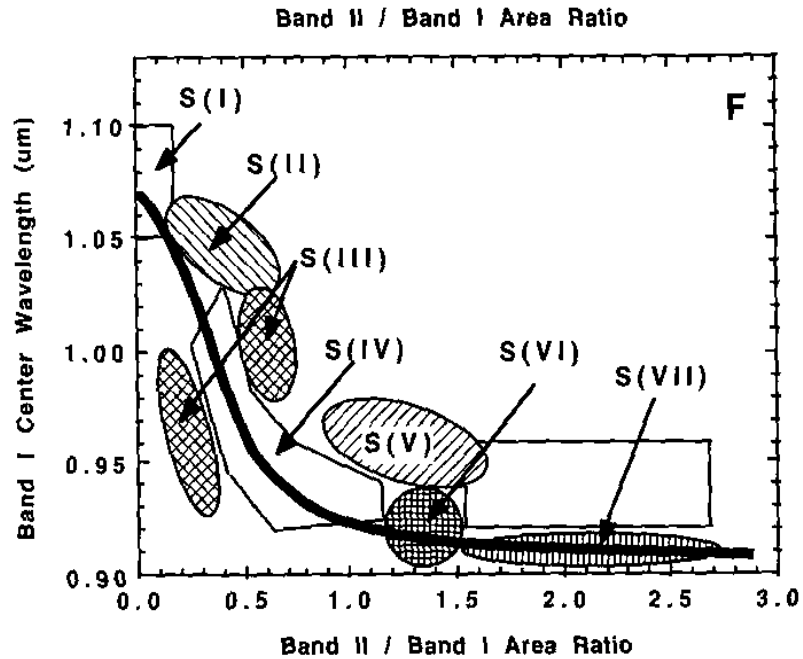


Figure 3.8 Mineralogical variation in the S-asteroid subtypes. (Gaffey et al, 1993)

A further example is seen with X-type asteroids. Prior to the introduction of the SpeX spectrograph at NASA's Infrared Telescope Facility X asteroids were considered spectrally featureless. The original Tholen (1984) taxonomic classification defined X-type asteroid by their featureless spectra and red-slopes; if albedo information is available this taxonomic class could be further divided into three subclasses: E-asteroids (high albedo), M- (moderate albedo) and P- (low albedo). Hardersen et al. (2011), taking advantage of the increased sensitivity offered by the SpeX instrument, demonstrated that significant mineralogical and spectral diversity exists amongst a group of 45 M-/X asteroids which were studied. Near infrared spectral reflectance measurements, in the wavelength range 0.75 to 2.5 microns, indicated the presence of diagnostic mineral absorption features for pyroxene(s), olivine, phyllosilicates and hydroxides in sixty percent of the asteroids observed.

## Chapter IV

### Observations and Data Reduction

Observations were made at NASA's Infrared Telescope Facility (IRTF), which is located on the summit of Mauna Kea at an elevation of 4160 m. The site exhibits superior atmospheric transmission characteristics making it suitable for near infrared observations which are particularly sensitive to the effects of telluric absorption. Figure 4.1 shows the typical atmospheric transmission at the summit of Mauna Kea for the wavelength range 0.9 to 2.7  $\mu\text{m}$ .

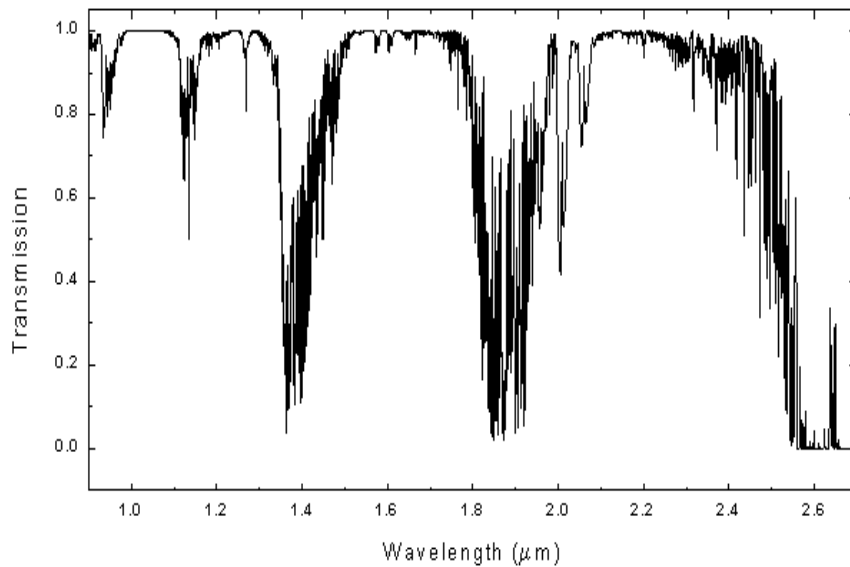


**Figure 4.1 Atmospheric transmission at the summit of Mauna Kea for the wavelength range 0.9 to 2.7 $\mu\text{m}$ . (Tom Geballe, Gemini Observatory) Assumptions: water vapor column of 1.6 mm and air mass of 1.0.**

The IRTF's is a 3.0 meter Cassegrain telescope optimized for infrared observations and supports multiple instruments (<http://irtfweb.ifa.hawaii.edu>). Observing at near infrared wavelengths is complicated by the fact that room temperature objects radiate in the near infrared region of the spectrum. Thus the design deliberately undersized the secondary mirror to prevent the instrument from seeing the thermal emission from the structure around the primary mirror. The mirror coatings were selected to have minimal thermal emission (Rayner et al. 2003).

Spectral measurements were made using the SpeX, a near infrared (0.8 to 5.5 micron), medium-resolution cryogenic spectrograph (Rayner et al., 2003, 2004). The SpeX is encased in a vacuum jacket, which is cryogenically cooled to minimize internally generated thermal infrared radiation. The spectrograph's optics are cooled to an operational temperature of 75 K using liquid nitrogen. The InSb detectors are cooled to 30 K using closed-cycle coolers. The design uses prism cross-dispersers and gratings to provide resolving powers up to  $R \sim 2000$ . A high-throughput, low resolution,  $R \sim 200$  prism mode is also provided for faint object and occultation spectroscopy (Rayner et al. 2003). The spectrograph was operated in low resolution mode in order to improve the signal to noise ratio (SNR). Asteroid NIR spectral absorption features are much broader than stellar spectral features so high resolution was not required. Figure 4.2 below shows a schematic of SpeX (Rayner et al. 2003). After splitting by the grating/prism the spectra are dispersed onto an Aladdin 3 1024 x 1024 InSb infrared detector array which has a spatial scale of 0.15" per pixel. Spectra are then read out of the array and recorded in Flexible Image Transport System (FITS) format (see figure 4.3).



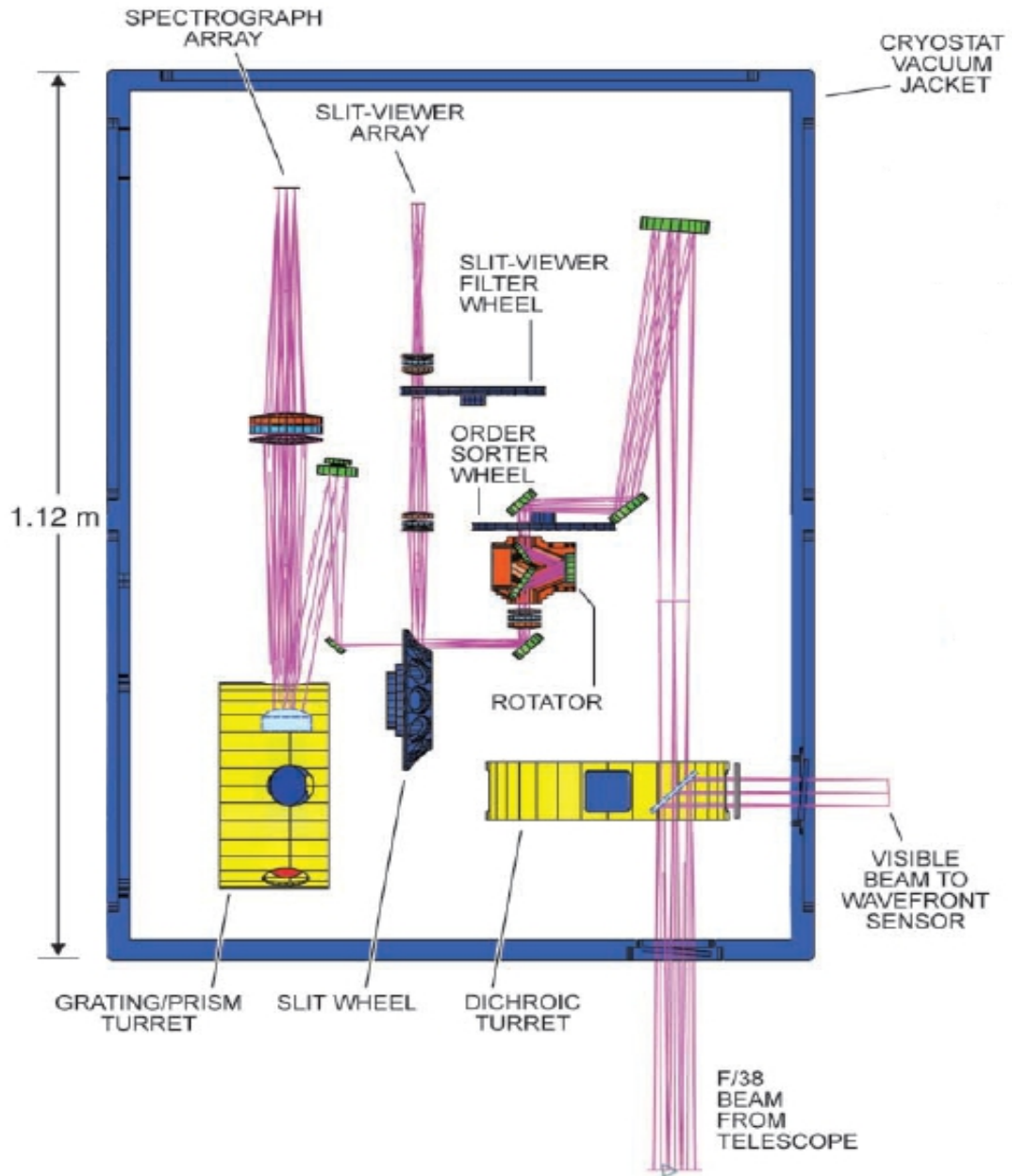


Figure 4.2 Schematic of the Spex Instrument (NASA IRTF)

Asteroid 2002 JB<sub>9</sub> was observed on the night of June 2<sup>nd</sup> 2011. Unfortunately the quality of the data was rather poor due to thick clouds (see figure 5.13 Observing Log) Even during clear periods the atmospheric transparency was poor due a transient cap cloud. Ideally we would like the amount of water vapor to be as low as possible to minimize the effects of telluric absorption. During the run, 2002 JB<sub>9</sub> had an apparent magnitude of 13.9, so a 120- second integration time was used for each spectrum. In total, 20 spectra were recorded. Observations of 2002 JB<sub>9</sub> were bracketed by observations of SAO 121593 a 9<sup>th</sup> magnitude extinction star of spectral type G5D (Skrutskie et al. 2006). SAO121593 is not a spectral type G2V star therefore a solar analog star, SAO 121593, was observed in order to correct for the non-solar spectrum.

Asteroid 3628 Božněmcová was observed on the night of June 4, 2011<sup>th</sup>. Atmospheric seeing of 0.7 arc seconds was recorded. Relative humidity varied from 47% to a high of 91%. In total, 38 spectra were recorded over an air mass values that ranged from 1.791 to 1.330. Each spectrum was integrated for 120 seconds. Asteroid observations were interspersed with observations of SAO 146077 a 9<sup>th</sup> magnitude extinction star of spectral type G5V. Since SAO 146077 is not a type G2V star a solar analog star SAO 157621 was observed in order to correct for the non-solar spectrum of the extinction star.

## Data Reduction

The raw *FITS* images were viewed and processed using *Image Reduction and Analysis Facility* (IRAF), a general purpose software package for reduction and analysis of astronomical data. Figure 4.3 shows a typical *FITS* image of a dispersed spectrum. Note that the asteroid's spectrum is dispersed over multiple rows on the SpeX IR array. While there are some hot pixels in each image, the majority of the bright white pixels in the image result from cosmic rays striking the detector. These cosmic ray hits are clearly visible as spikes in figure 4.4, which plots the raw count (flux) verse channel number. The number of cosmic ray hits was, understandably, higher on the images with longer integration times.

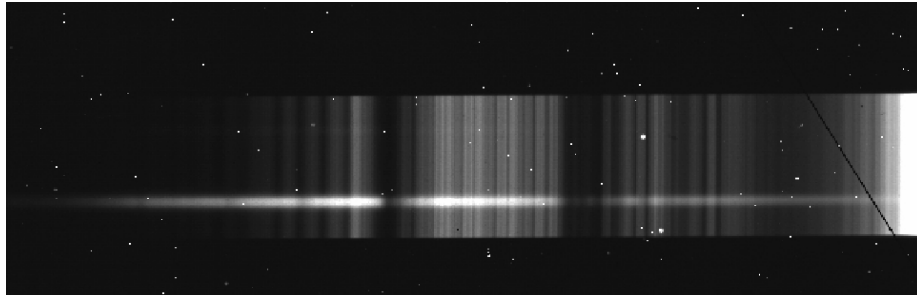


Figure 4.3 FITS image showing the raw spectrum of asteroid 2002 JB<sub>9</sub>.

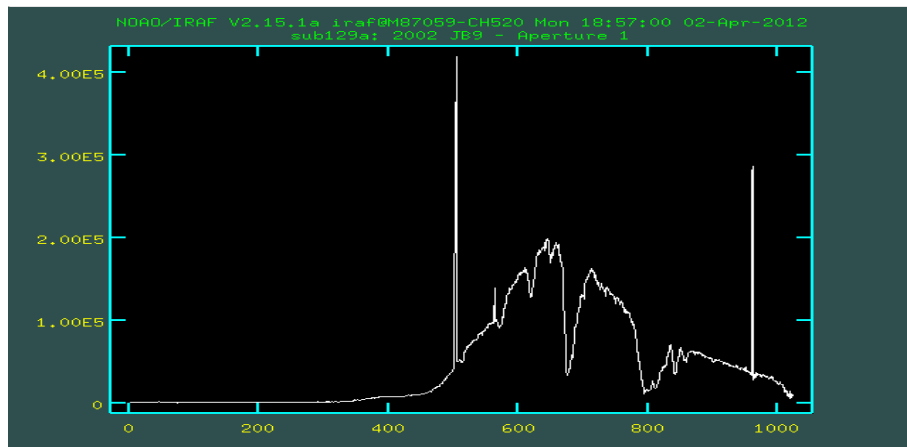
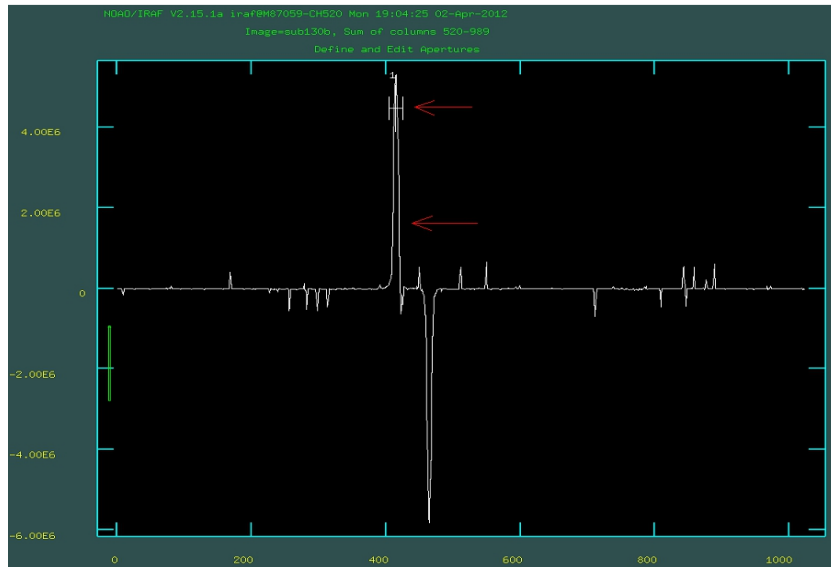


Figure 4.4 IRAF plot of raw pixel count (flux) verses channel number.

In order to remove the bias and background sky noise from the images, observations of equal integration time were captured in pairs, each on a different part of the detector, and then subtracted using the IRAF *imarith* (binary image arithmetic) function. The positive and negative peaks seen in Figure 4.5 are the result of this subtraction operation.



**Figure 4.5** Determination of the aperture center using the IRAF *apall* routine.

To extract the dispersed spectrum from the FITS images it was first necessary to define an extraction aperture, which encompassed those detector rows containing the maximum spectral flux. This was accomplished using IRAF's *apall* routine. In figure 4.5 above you can see the peak intensity rows (positive peak) are bracketed by an aperture (the H symbol numbered 1). The width of the extraction aperture was configurable in the associated parameter file and was generally set to somewhere in the range of  $\pm$  5- to 10 pixels. As the IRTF telescope slews across the sky the IR array in the SpeX instrument experiences a small amount of gravitationally induced flexing. This causes the position of

dispersed spectra to vary across the surface of the IR array; the maximum variation is on the order of one or two pixels. To correct for this effect IRAF's *apextract* function fits a curve to the maximum flux data points prior to extraction. The extracted spectra were then converted to .txt format using the *listpix* routine, which also truncated the first 349 channels which do not contain valid flux information. This data was then exported to SpecPR<sup>9</sup> for further reduction and analysis. In SpecPR one can perform various functions such as averaging of spectra, creating star packs or removing telluric features.

Wavelength calibration was achieved using the spectrograph's internal argon lamp. An averaged emission line spectrum (Figure 4.6) was generated and the channel numbers corresponding to the emission peaks were identified. This data was exported to MS Excel and a polynomial curve was fitted. The polynomial curve's equation was then entered into the SpecPR as a wavelength calibration file.

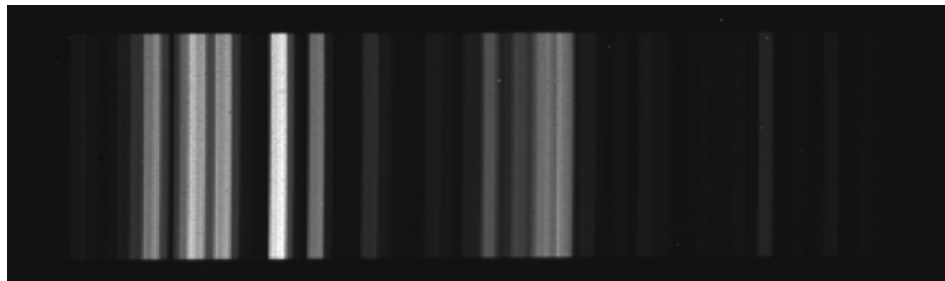


**Figure 4.6 Argon emission line spectra captured on the spectrograph array.**

---

<sup>9</sup> SpecPR is a data reduction and analysis package for IR spectra written by Clark (1980) and Gaffey (2003).

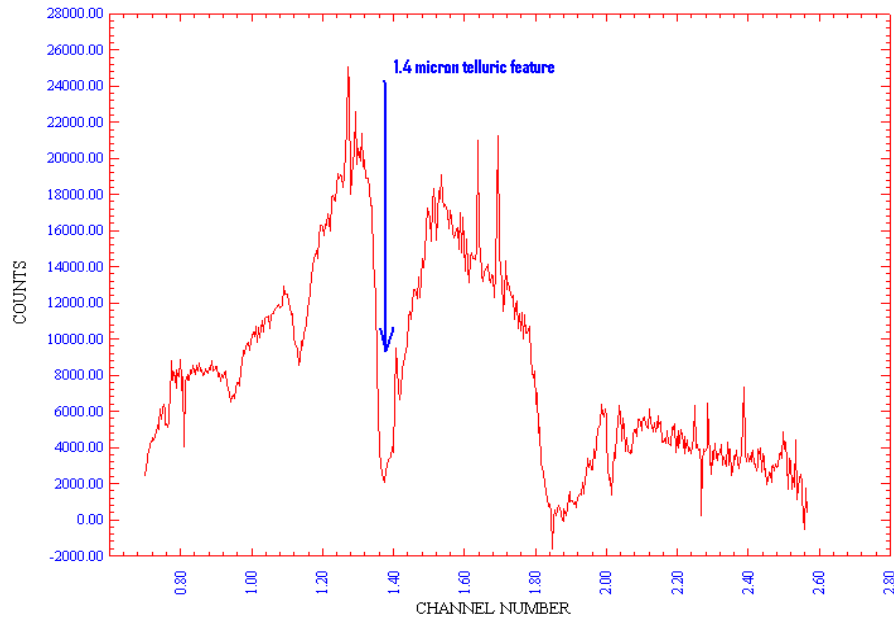


**Figure 4.7 A single, raw, spectrum of Asteroid 3628 Božněmcová.**

Figure 4.7 shows a plot from SpecPR of the raw flux versus wavelength for asteroid 3628 Božněmcová. Note the strong absorption features at 1.4 microns and 1.9 microns and weaker features at 0.94 and 1.00 microns which are due to atmospheric water vapor.

To produce a reflectance spectrum it was first necessary to remove these telluric absorption features. This was achieved by dividing each asteroid spectrum by a “starpack”. The starpack is essentially a set of wavelength dependent extinction coefficients which accurately model the wavelength dependent atmospheric transmission and particularly the shape, depth, and width of the telluric features at 1.4 and 1.9 microns. The starpack is generated from observations of an “extinction star” chosen to be as close in the sky to the asteroid which, ideally, means both the star and asteroid are observed under similar atmospheric conditions.

During the observing run each set of asteroid observations was bracketed by observations of the extinction star and the extinction star observations were used to create the starpack. Calculation of the starpack involved generating a plot of the log of flux versus the airmass as seen in Figure 4.8. This plot was then fitted with a linear regression to derive the slope and intercept of the distribution. This process was repeated for each wavelength in the observations. The starpack is then used to calculate the wavelength dependent flux of the standard star at exactly the same airmass as each individual asteroid observation, removing the effects of atmospheric absorptions and resulting in the asteroid/star ratio.

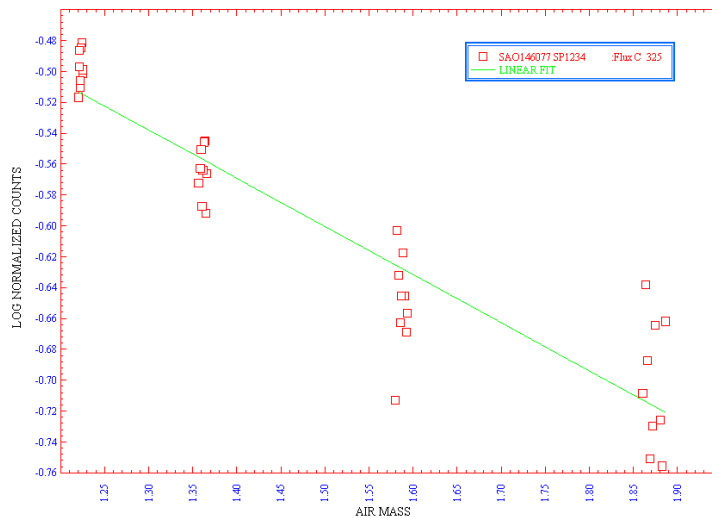


**Figure 4.8 Plot of the log of standard star flux verse air mass.**

When generating the starpack it was necessary to address the problem of the spectra being shifted on the IR array due to the instrument flexing as the telescope slewed back and forth between the asteroid and standard star. To correct for this effect each set of standard star observations was channel shifted against the initial reference set. Failure

to do this would have resulted in artifacts being introduced into the final reduced spectrum.

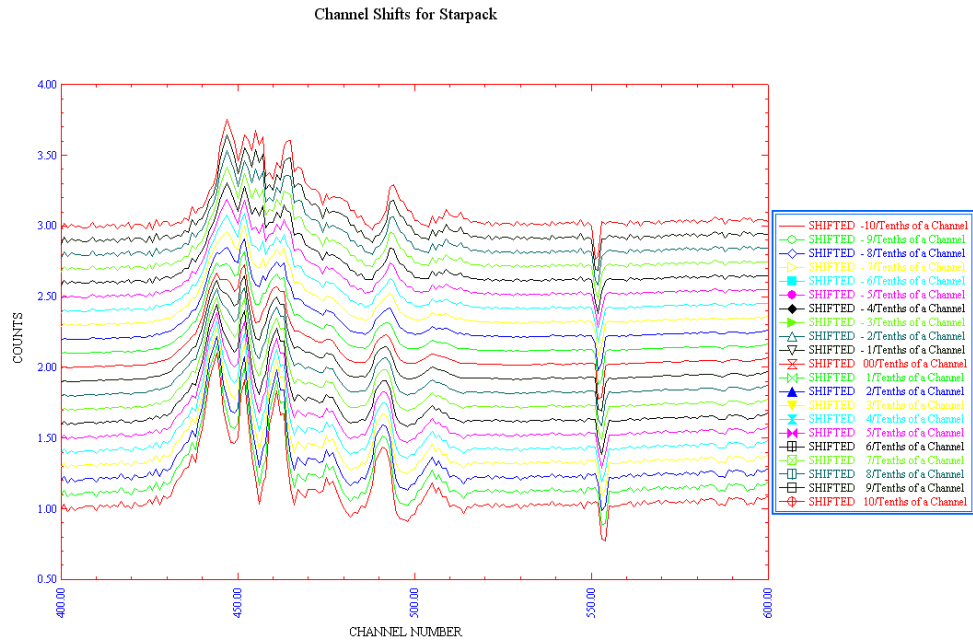


**Figure 4.9** Spec PR plot showing the effect of progressively channel shifting the standard star spectra by 1/10 of a channel.

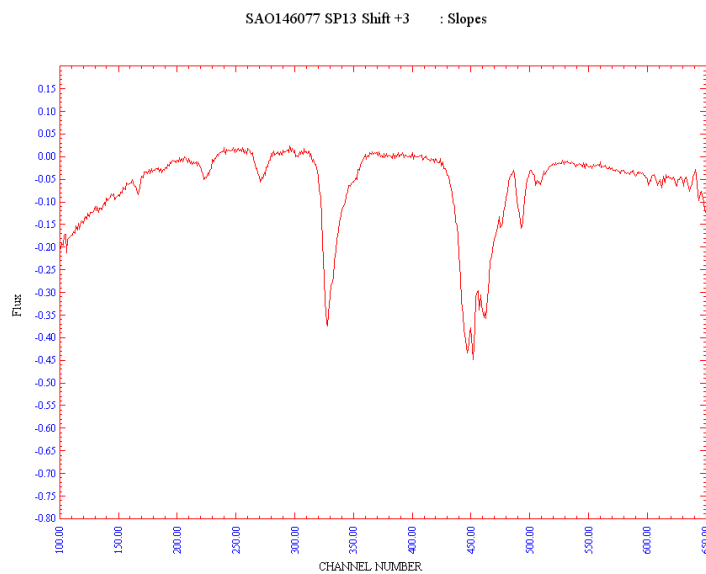


**Figure 4.10** Slope of the starpack used to remove telluric features from 3628 Božněmcová.



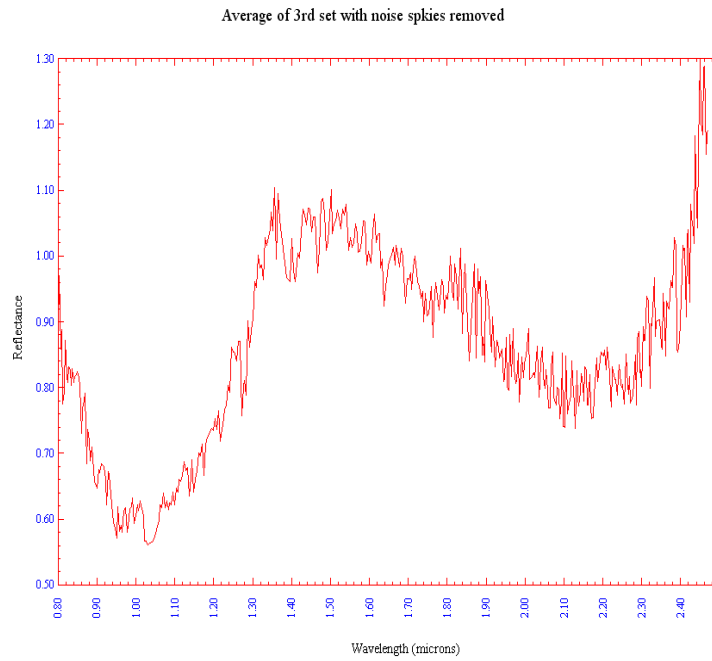


**Figure 4.11** Resulting average of 7 spectra of 3628 Božněmcová/divided by starpack.

In order to improve the signal to noise ratio the spectra were averaged together and data points beyond one standard deviation were removed. SAO 146077, the extinction star used, is not a type G2V star, thus an additional solar analog star SAO 157621 (Skrutskie et al. 2006) was also observed in order to correct for the non-solar spectrum of the standard star. The final spectrum was produced by dividing asteroid spectra/starpack by the average solar analog/starpack.

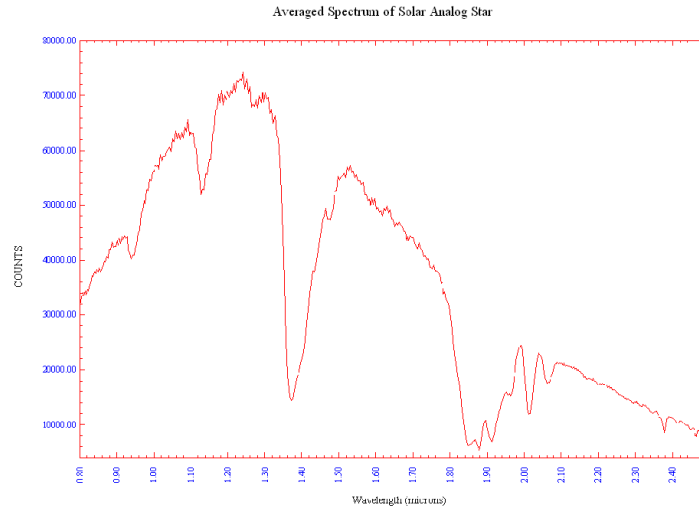


**Figure 4.12 Averaged Spectral Flux curve of Solar Analog Star SAO157621**

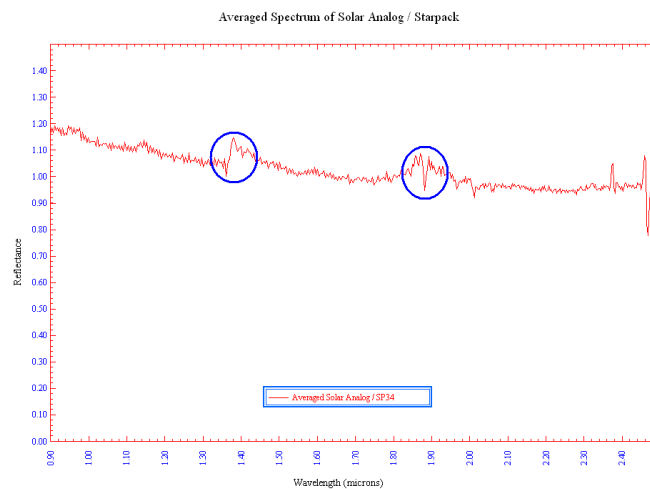


**Figure 4.13 Solar Analog Star/Divided by Starpack.**

Note the residual water features at 1.4 and 1.9 microns in figure 4.13 above (circled in blue). They are the result of imperfect atmospheric correction which was most likely due to the highly variable relative humidity on the night. Figure 4.14 shows the final spectrum of 3628 Božněmcová. It was interesting to see that the 2 micron feature became considerably weaker once the spectrum was corrected to account for the non-solar spectrum of the standard star. .

Asteroid 3628 Božněmcova - Final Spectrum

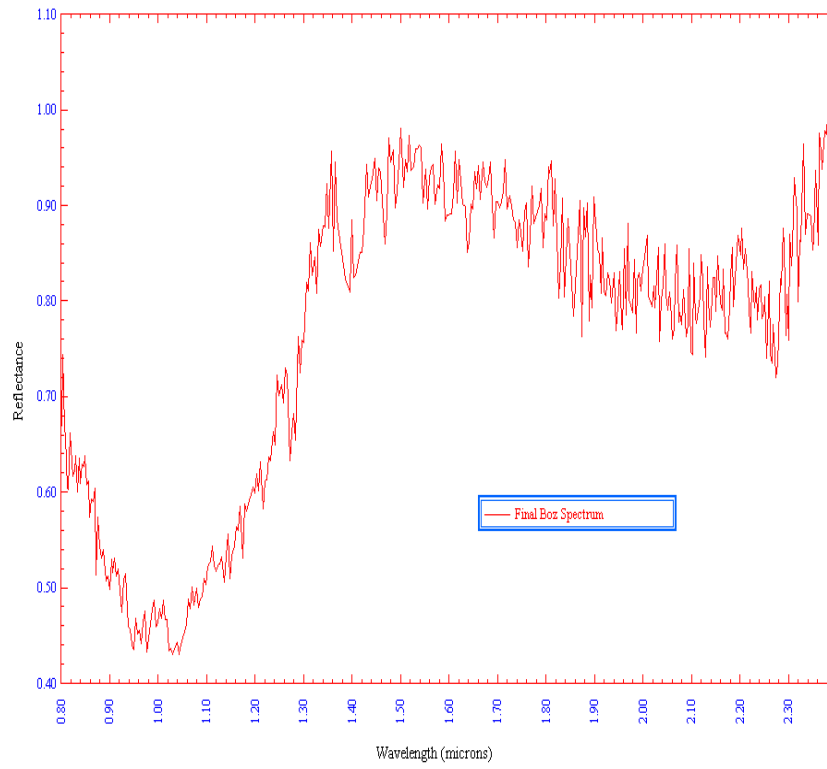


Figure 4.14 Final spectrum of asteroid 3628 Božněmcová

## Chapter V

### Data Analysis and Interpretation

#### 5.1 Data Analysis

It is possible to constrain an asteroid's silicate mineralogy by measuring the center wavelengths of the Band I and Band II absorption features, (figure 5.1) which are functions the mineral's crystal structure. This is usually visually presented on a plot of the Band I Center vs. the Band II Center (i.e. Adams, 1974, Gaffey 2011) (figure 5.12). These may then be utilized to determine the average pyroxene or olivine chemistry. Calculating the ratio of the areas within the Band I and Band II absorption features yields the relative abundance of olivine and pyroxene.

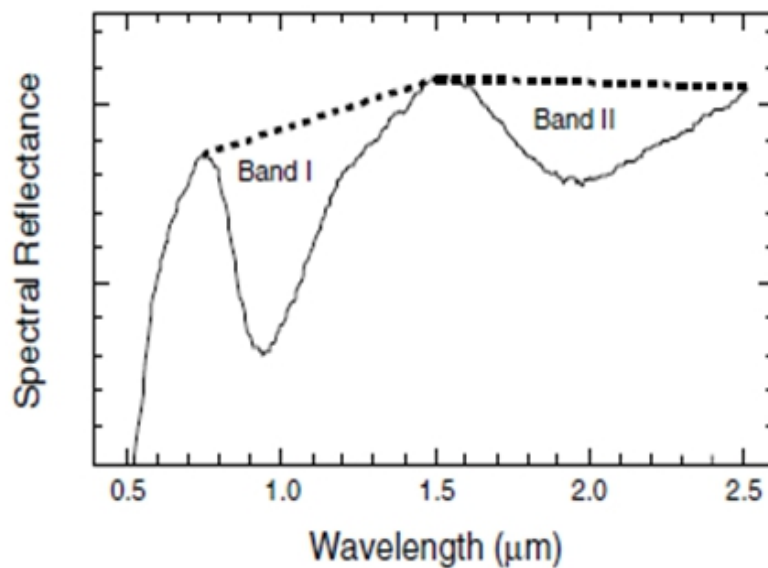
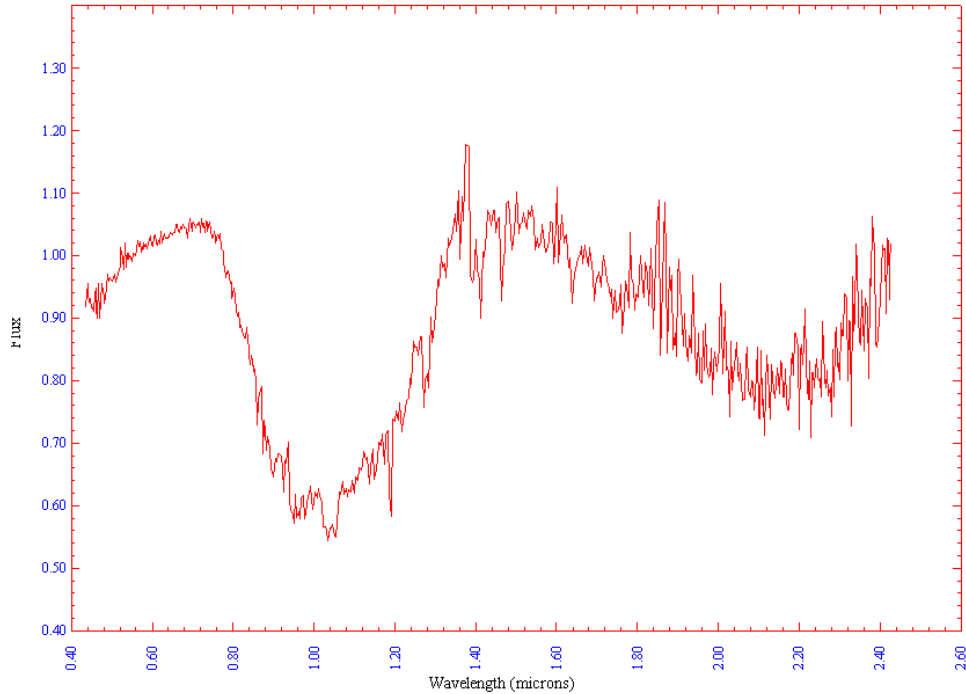


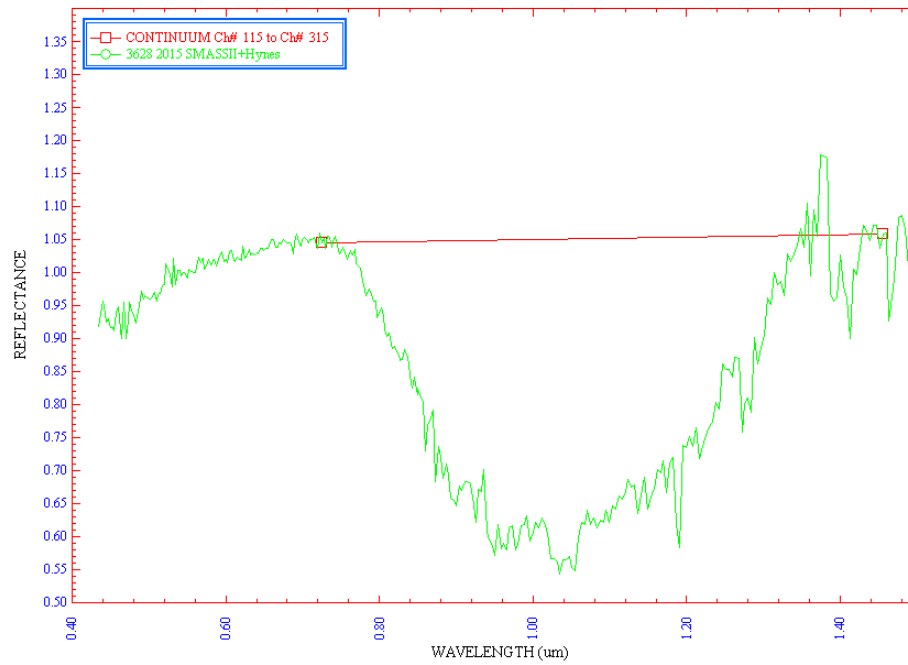
Figure 5.1 Diagnostic Spectral Parameters. From *Mineralogy of Asteroids* (Gaffey et al (2002)).



## 5.2 Combined Hynes 2011 and SMASS spectrum for 3628 Boznemcova

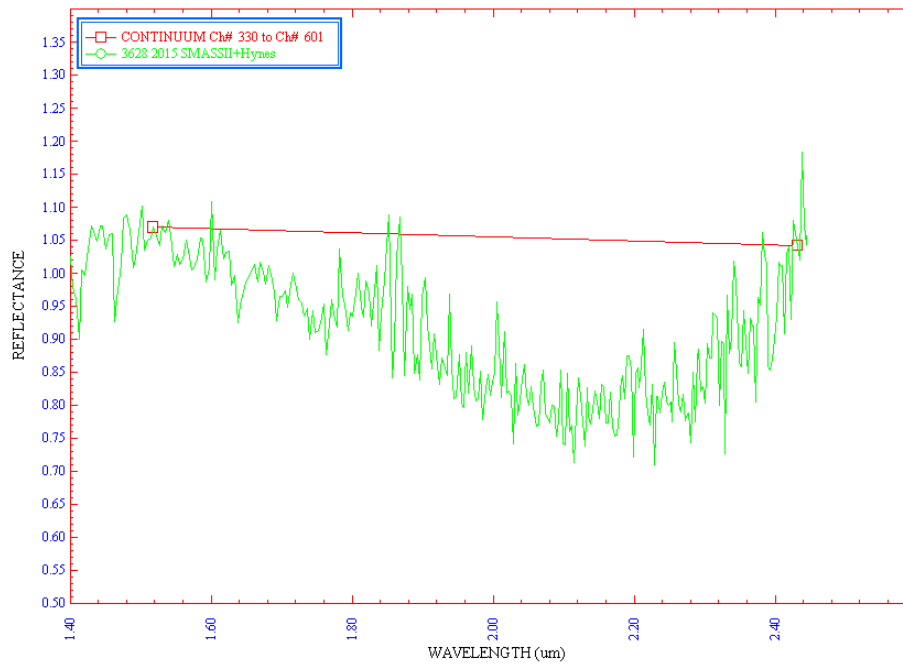
In order to gain more complete coverage of the 1 micron absorption feature the spectrum of 3628 Boznemcova obtained from the IRTF observations was merged with an earlier visible/NIR spectrum from the SMASS survey (figure 5.2). The SpecPR software package contains routines that permit calculation of the normalized band area of an absorption feature using a linear continuum fit across the absorption feature as a proxy for the actual spectral continuum. While not strictly accurate it allows asteroid and meteorite spectra to be compared. Due to noise in the spectrum it was not possible to determine the exact beginning and end points of the absorption features thus multiple iterations of the linear continuum fit, each having slightly differing start and end points, were made. Figures 5.3 and 5.4 show examples of this iterative process.

Continuum Fit to Band 1



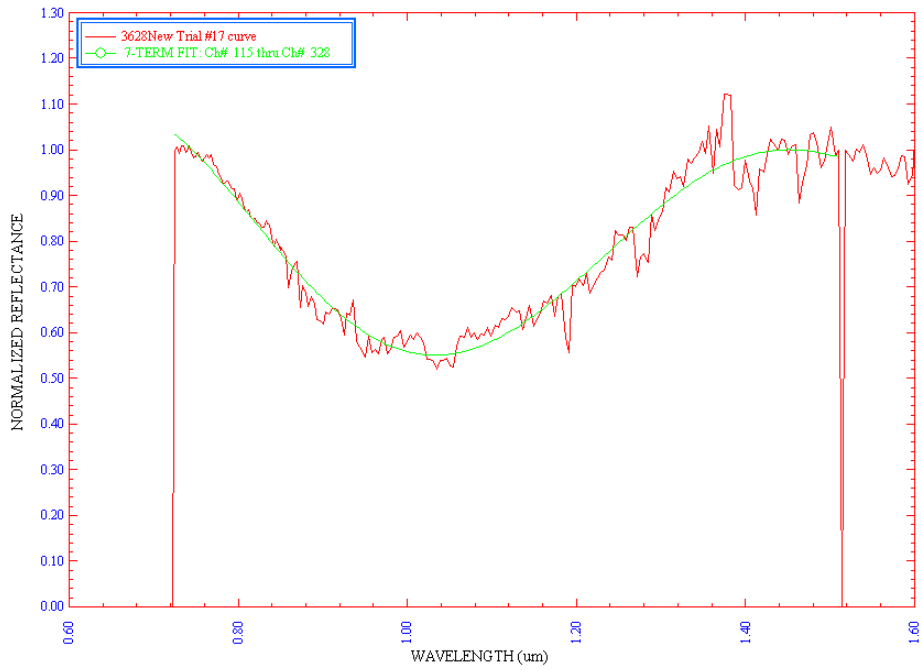
### 5.3 Linear continuum fit to the Band 1 feature of 3628 Božněmcová

Continuum Fit to Band 2



### 5.4 Linear continuum fit to the Band 2 feature of 3628 Božněmcová

Polynomial Fit to Band 1



5.5 Polynomial fit to the 1 micron feature

Polynomial Fit to Band 2



5.6 Polynomial fit to the 2 micron feature

The SpecPR software will also allow one to fit a polynomial function to a feature in order to determine the band center. Again, due to the noisy nature of the spectrum, multiple iterations of the polynomial fit were made. Figures 5.5 and 5.6 show examples of the polynomial fits to the band I and band II features.

The Band I center was determined to be  $1.02 \mu\text{m} \pm 0.06$  while the Band II center was determined to be  $2.158 \mu\text{m} \pm 0.08$ . Due to excessive noise, data beyond 2.4 microns was removed prior to calculation of the band areas. The normalized Band Area for the  $1 \mu\text{m}$  feature was 0.176 while the normalized Band Area for the  $2 \mu\text{m}$  feature was 0.107; this was based on 24 iterations. This gave a Band Area Ratio equal to 0.612.

## **5.2 Interpretation of asteroid 3628 Božněmcová spectra**

Over the past two decades a number of mineralogical interpretations have been proposed for asteroid 3628 Božněmcová. Binzel et al. (1993) measured the visible/near IR reflectance spectrum over a limited wavelength range from 0.5 to 1.0 microns (Figure 5.7) and suggested that the spectrum was similar to a near Earth asteroid, 1862 Apollo. 1862 Apollo had previously been identified as a potential source body for ordinary chondrite meteorites, which constitute the bulk of meteorites falls (McFadden et. al, 1985). The proximity of 3628 Božněmcová to the 3:1 Kirkwood gap suggested it might actually be a “possible parent body” source for the ordinary chondrites meteorites. “Possible” parent bodies have a mineralogy which matches a particular meteorite type while “probable” parent bodies have both the correct mineralogy and are located in an orbit where they can contribute Earth-crossing material.



Follow up observations, made over a wider wavelength range of 0.35–1.65 microns, showed that the spectral similarity with ordinary chondrites did not continue beyond 1.2 microns (Figure 5.8). Burbine and Binzel (2002) refuted the previously proposed match to ordinary chondrites meteorites contending that the structure of the 1- $\mu\text{m}$  band is unlike any currently known meteorite. They conceded that extended spectral coverage, to 2.5 microns, was needed to support this claim.

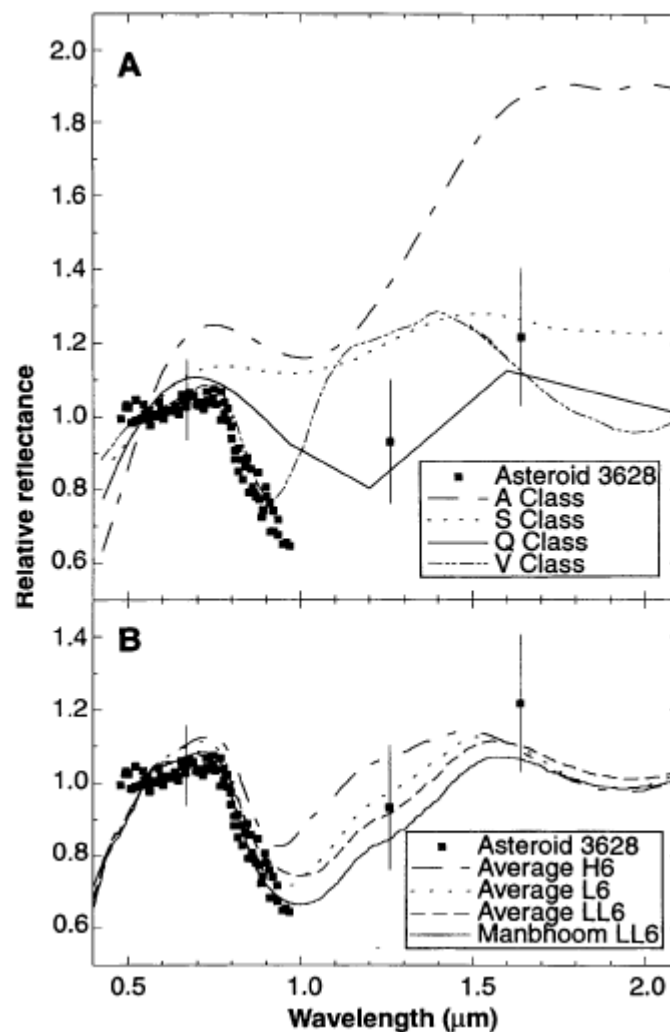
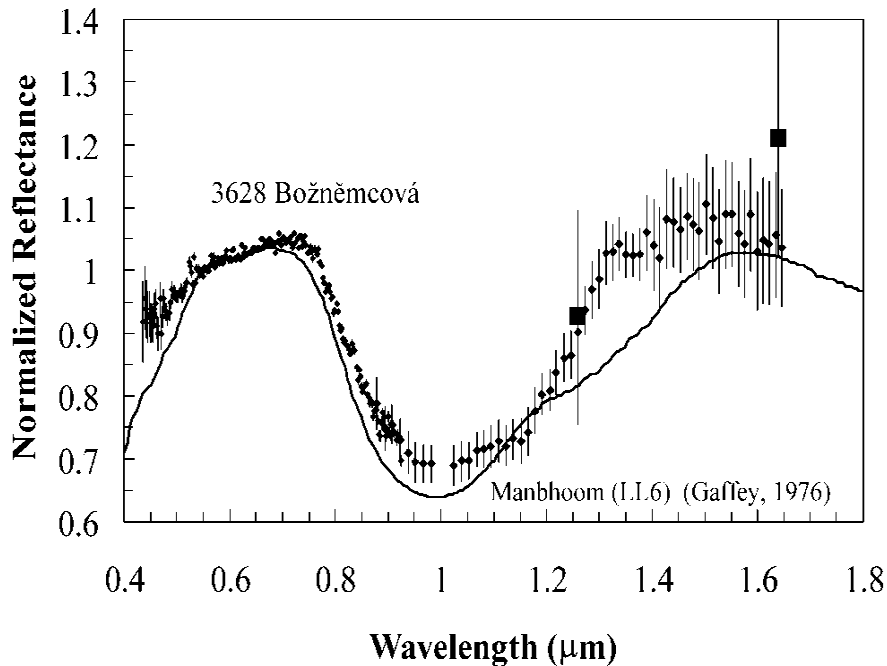
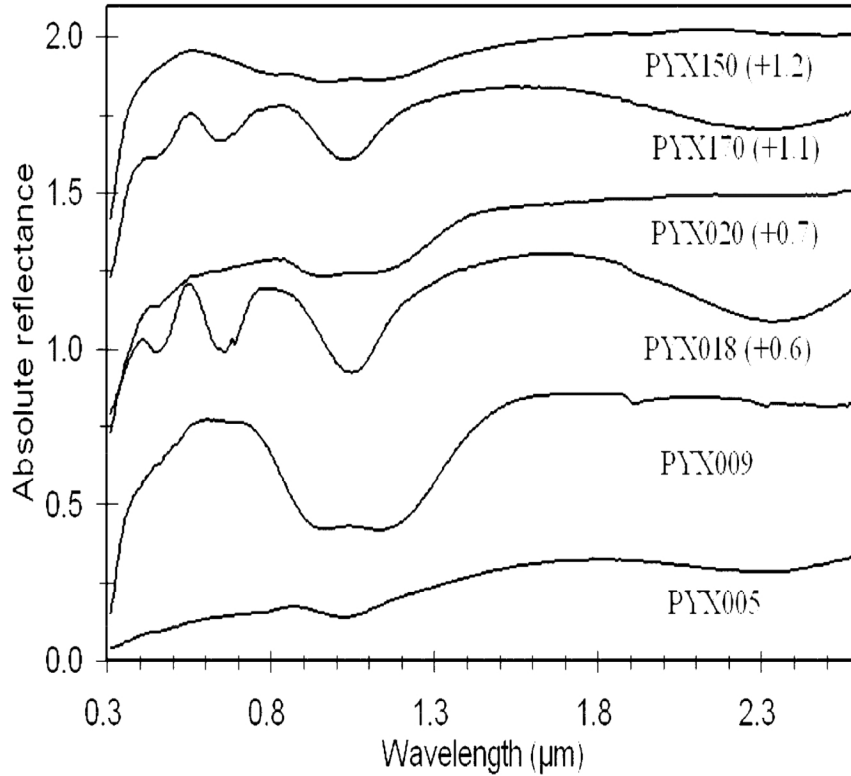


Figure 5.7 Visible/near IR spectrum of 3628 Božněmcová compared to spectra of ordinary chondrite meteorites. (Binzel et al, 1993).



**Figure 5.8 Normalized reflectance spectrum of 3628 Božněmcová compared to an LL6 ordinary chondrite. (Burbine and Binzel, 2002).**

Cloutis et al. (2006) proposed that 3628 Božněmcová had a surface mineralogy that includes a type A clinopyroxene with a ferrosillite content in the range ~10–20% with 90% of the  $\text{Fe}^{2+}$  being present in the M1 crystallographic site (spectral type A). Type A clinopyroxene is typified by spectra containing a broad 1  $\mu\text{m}$  feature that is actually composed of two overlapping absorption bands near 0.95 and 1.15 microns. These are attributable to crystal field transitions in the  $\text{Fe}^{2+}$  cation located in the M1 crystallographic site. In contrast, spectral type B clinopyroxenes are characterized by two major absorption bands located near 1 and 2.2  $\mu\text{m}$  that are attributable to crystal field transitions in  $\text{Fe}^{2+}$  located in the M2 crystallographic site (Cloutis et al., 2006)



**Figure 5.9 Laboratory reflectance spectra (0.3–2.6  $\mu\text{m}$ ) of three pairs of type A and type B clinopyroxenes. PYX 150, PYX020 & PYX009 are type A. PYX170, PYX018 & PYX005 are type B. (Cloutis et al., 2006).**

Two distinct absorption features, centered at 1.02 and 2.16 microns, are clearly visible in the final spectrum of 3628 Božněmcová (figure 5.2). There is a slight difference in the position of the band two centers between the 2007 and 2011 spectra. This may be due variation in the surface mineralogy as the asteroid rotates. The presence of both 1 and 2 micron absorption features is consistent with the presence of type B clinopyroxene and 3628 Božněmcová plots along the calcium pyroxene trend line on the pyroxene Band I versus Band II plot shown in Figure 5.12, which indicates the presence of high calcium pyroxene component plus an additional, unidentifiable, mineral phase. High calcium

pyroxene is a spectrally detectable and petrologically important indicator of igneous history being one of the most effective tracers of melting of a chondritic precursor (Sunshine et al, 2004).

When the band centers and band area ratio were entered into the pyroxene calculator the results for 3628 Božněmcová (see appendix II) were as follows: the pyroxene chemistry is 46.4 mol percent of Wollastonite and 23.9 percent Ferrosillite. In terms of finding a corresponding terrestrial meteorite analogue for 3628 Božněmcová it has been speculated that it may be amongst the angrites. Angrite meteorites are medium to coarse grained (up to 2-3 mm), unbrecciated and substantially unshocked igneous rocks of roughly basaltic composition. They are composed predominantly of anorthite, Al-Ti diopside-hedenbergite, and Ca-rich olivine (Mittlefehldt et al., 2002). This abundant olivine phase in D'Orbigny and Sahara 99555 produces the characteristic olivine spectral curve. The weak 2 micron pyroxene band observed in some angrites is characteristic of high-Ca pyroxene where the  $Fe^{2+}$  is located almost entirely in the M1 crystallographic site. Oxygen isotope measurements indicate that all measured angrites have originated from the same parent body or at least from the same oxygen isotopic reservoir (Greenwood et al. 2005).

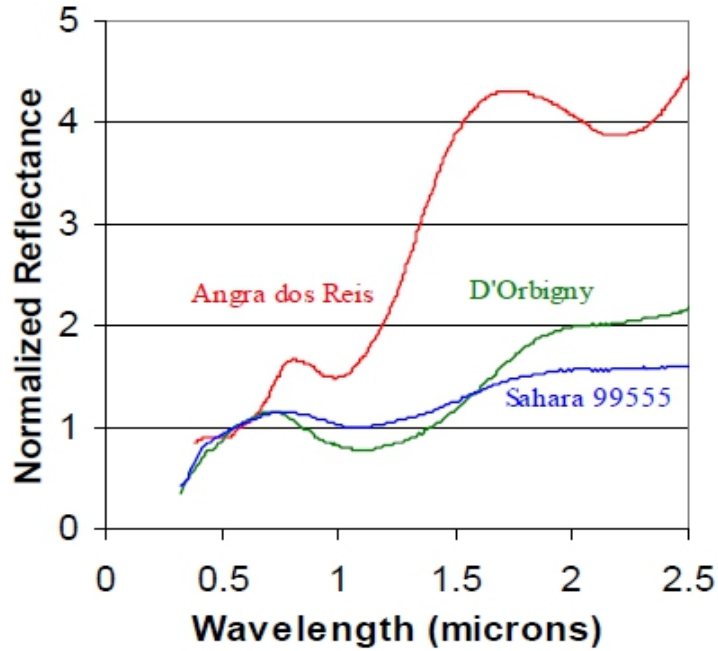


Figure 5.10 Spectra of angrite meteorites (Burbine et, 2001). Spectra normalized to unity at 0.55  $\mu\text{m}$

### Comparison Plot of Angra-Dos-Reis & 3628 Boznemcova

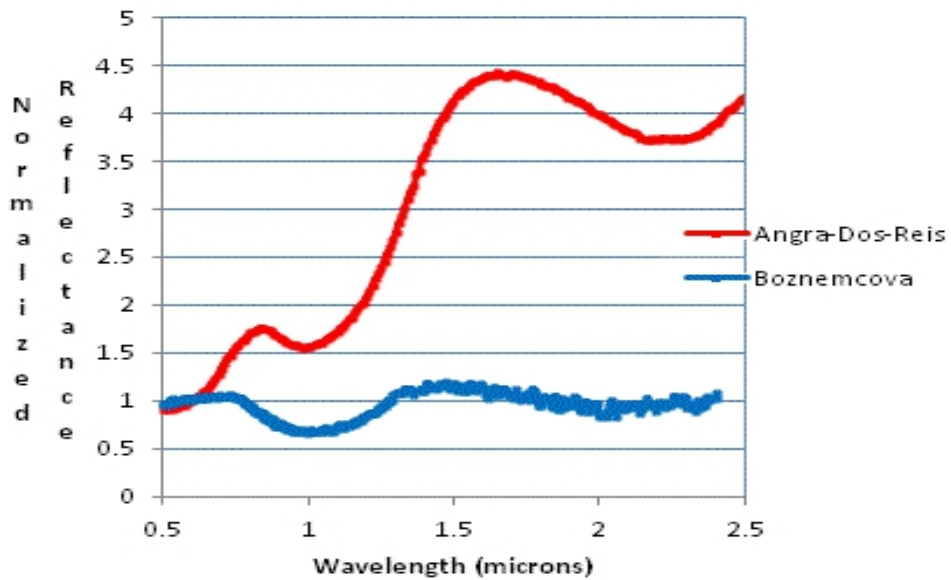


Figure 5.11 Comparison of Angra Dos Reis & Boznemcova Spectra. (Normalized to unity at 0.55  $\mu\text{m}$ )

The closest match amongst the angrites (figure 5.10) would appear to be Angra dos Reis; the majority of meteorites in this class have either very weak or totally absent 2 micron absorption features (Burbine et al., 2006). Angra dos Reis has a spectrum characterized by a very sharply increasing infrared reflectivity with two strong features centered at about 1.0 and 2.25 microns, which are indicative of the presence of augite-diopside (Adams, 1974a). Analysis of Burbine's 2001 spectrum in SpecPR show band centers at 1.04 and 2.19 microns.

Angra Dos Reis consists almost entirely of fassaite pyroxene, a type of clinopyroxene that is rich in aluminum and titanium—elements that normally do not readily enter pyroxene (Jones et al., 2005). The fassaite in angrites are calcic diopsides with typically 50 mole percent of the calcium component (wollastonite). Analysis of the spectral parameters obtained from SpecPR showed a wollastonite content of 54.8 mole percent as compared to 46.4 mol percent for 3628 Božněmcová. While not entirely conclusive, the implied mineralogy for 3628 Božněmcová, i.e. a high calcium type B clinopyroxene with a possible fassite component, suggests it should not be ruled out as a possible parent body for the angrite meteorites. However, higher quality spectra taken over a full rotation period will be required to validate this interpretation.

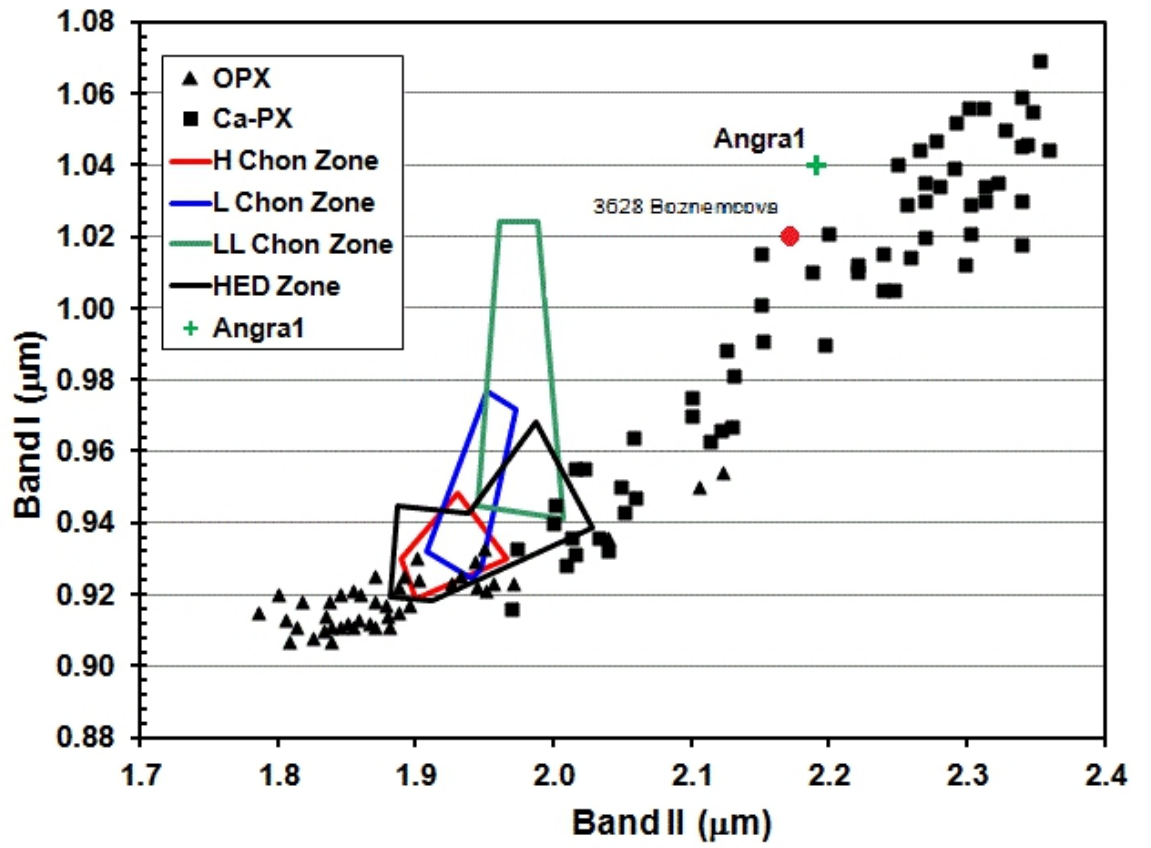


Figure 5.12 Band 1 vs. Band 2 plot of 3628 Boznemcova and Angra Dos Reis

## 5.2 Analysis and Interpretation of asteroid 2002JB<sub>9</sub>

The presence of transient cloud cover (see figure 5.13 – observing log) at the summit of Mauna Kea degraded the atmospheric transparency to the extent that almost half of the spectra were discarded due to very low or un-useable signal to noise ratios. Even during the comparatively clear periods the relative humidity was still high and quite variable. This variability resulted in a poor atmospheric correction, thus residual 1.4 and 1.9 micron water vapor features are still present in the spectra (figure 5.16)

| Target               | Type                      | No. of Spectra | Exp. Time (sec) | Start-End No.   | Airmass | Actual UT Start | Comments                     |
|----------------------|---------------------------|----------------|-----------------|-----------------|---------|-----------------|------------------------------|
| Data Path>>          | scrs1/bigdog/Reddy/June02 |                |                 |                 |         |                 | All obs at parallactic angle |
| Arcs/Flats           | Flat                      |                |                 | flat0001a-0005a | 1.004   | 5:20            | Focus 1.09, RH 49%           |
|                      | Arc                       |                |                 | arc0006a        | 1.005   | 5:22            | Seeing 0.6", Thick Clouds    |
| SAO141267            | Solar Analog              | 10             | 1               | spec0047a-0056b | 1.301   | 7:57            | Focus 1.07, Seeing 0.53"     |
| SAO121593            | Local Standard            | 10             | 3               | spec097a-0106b  | 1.114   | 8:36            |                              |
| 2002 JB <sub>9</sub> | PHA                       | 20             | 120             | spec0117a-0136b | 1.103   | 8:55            | RH 67% :(                    |
| SAO121593            | Local Standard            | 10             | 3               | spec0137a-0146b | 1.033   | 9:51            |                              |
| SAO141267            | Solar Analog              | 10             | 1.5             | spec0167a-0176b | 1.066   | 10:25           |                              |
| SAO121593            | Local Standard            | 10             | 3               | spec0197a-0206b | 1.054   | 10:40           |                              |
| SAO141267            | Solar Analog              | 10             | 3               | spec0317a-0326b | 1.259   | 12:25           | RH 75% :(                    |
| Flats/Arcs           | Flat                      |                |                 | flat0327a-0331a | 1.284   | 12:32           |                              |
| Flats/Arcs           | Arc                       |                |                 | arc00332b       | 1.285   | 12:35           |                              |

**Figure 5.13 Observing log for 2002JB<sub>9</sub>**

Based on the data available it would appear that the spectrum of NEA 2002JB<sub>9</sub> contains no discernible diagnostic absorption features which could be attributed to simple mixtures of mafic silicates. Therefore it is possible to rule out olivine and pyroxene surface mineralogies. There is a very weak feature near 0.98 micrometers and possibly a broad shallow Band II feature but both are too weak and the signal to noise ratio of the spectra too low to permit reliable determination of the band centers (Gaffey, personal communication 2013). An essentially featureless spectrum could indicate a number of other potential surface mineralogies.



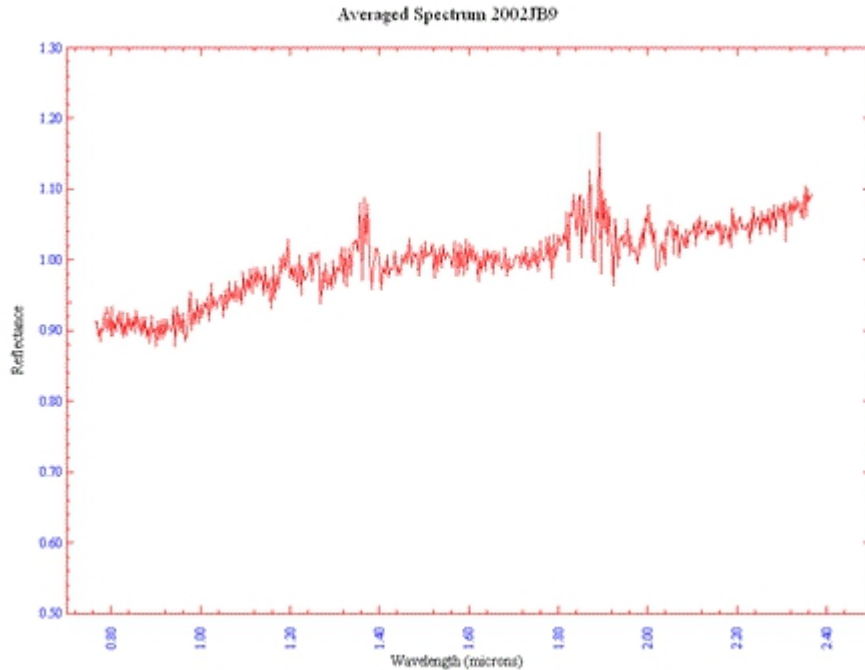


**Fig 5.14 Spectrum of NEA 2002 JB<sub>9</sub>.**

Hicks et al. (2011) made broadband photometric measurements of 2002 JB<sub>9</sub> and suggested, based on the mean colors ( $B-R = 1.114 \pm \pm 0.010$  mag;  $V-R = 0.392 \pm \pm 0.008$  mag;  $R-I = 0.374 \pm \pm 0.006$  mag) that it be classified as an X- asteroid. The extremely shallow solar phase curve<sup>10</sup> generated from photometry (Figure 5.15) was best fit with a phase parameter  $g = 0.91$ , consistent with a high albedo E-type spectral classification. The phase/albedo relationship discussed by Belskaya and Shevchenko (2000) suggests that the albedo of 2002 JB<sub>9</sub> may be as high as 0.8-0.9. A surface composed of enstatite achondrite material would correlate with the weakly featured spectrum however enstatites typically do not have such high albedos. Gaffey (1976) measured the spectra of three enstatite achondrites (aubrites). One contained dispersed dark F-chondrite grains and had an albedo of ~20%. The other two had minor rust stains

---

<sup>10</sup> An asteroid's phase curve is a plot of brightness as a function of solar phase angle.

and albedos of 42 & 50%. Burbine et al. (2002) reported albedos of 41 to 53% for three aubrites. Since even the most pristine aubrites contain traces of terrestrial weathering products (rust), their intrinsic albedos would be considerably higher, in theory nearly 100%. Ice would match the albedo, but there should be very strong absorption features near 1.5 and 2.0  $\mu\text{m}$  which are clearly absent.

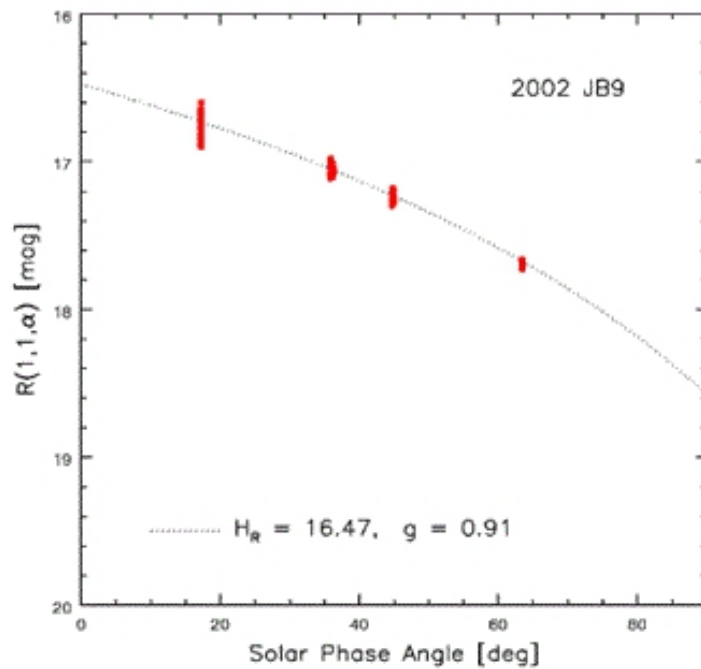


**Figure 5.15 Solar phase curve for 2002JB9 (Hicks et al., 2011).**

The spectra of iron and nickel-iron meteorites all have the same general form, an un-featured curve with reflectance increasing smoothly toward longer wavelengths (Cloutis, 2010). However this is only true for smooth / polished surfaces (Cloutis et al. 2010). The metallic NiFe surfaces on asteroids are likely to be rough and/or loose fragments neither of which has a high albedo. It is also possible to detect crystalline silica minerals, which do not contain any iron or feature producing transition metal species, if spectroscopy is extended into the mid infrared wavelengths. At thermal

infrared wavelength stretch and bend vibrational motions in crystalline silicate minerals produce emission features at 10 and 20 microns. However, in order for this phenomenon to occur the surface grains must be warm enough to emit in the IR. This places a fundamental limit on the distance from sun over which observations can be made. Luckily the surface of 2002JB9 is warm enough for this technique.

## Chapter VI

### Summary

The derived mineralogy for asteroid 3628 Božněmcová seems to be consistent with a high calcium, type B, clinopyroxene with a possible fassite component. This coupled with the fact that 3628 Božněmcová orbits close to the 3:1 Kirkwood gap suggests that it should not be ruled out as a possible parent body for the angrite meteorites.

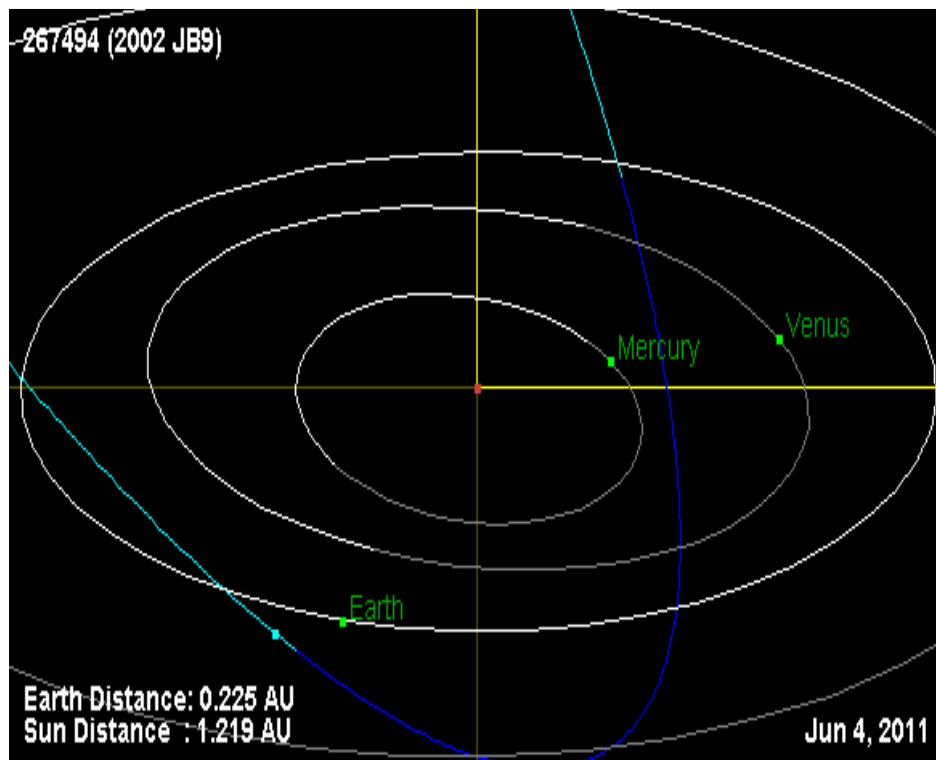
The spectra for 2002JB<sub>9</sub> contains only very weak features and no discernible diagnostic features in either the visible or near infrared that might be indicative of a mafic mineralogy. The essentially flat, featureless, spectrum and extremely high albedo is suggestive of an enstatite surface mineralogy. Unfortunately, the poor quality of the data makes this determination less than certain.

### Recommendations for further work

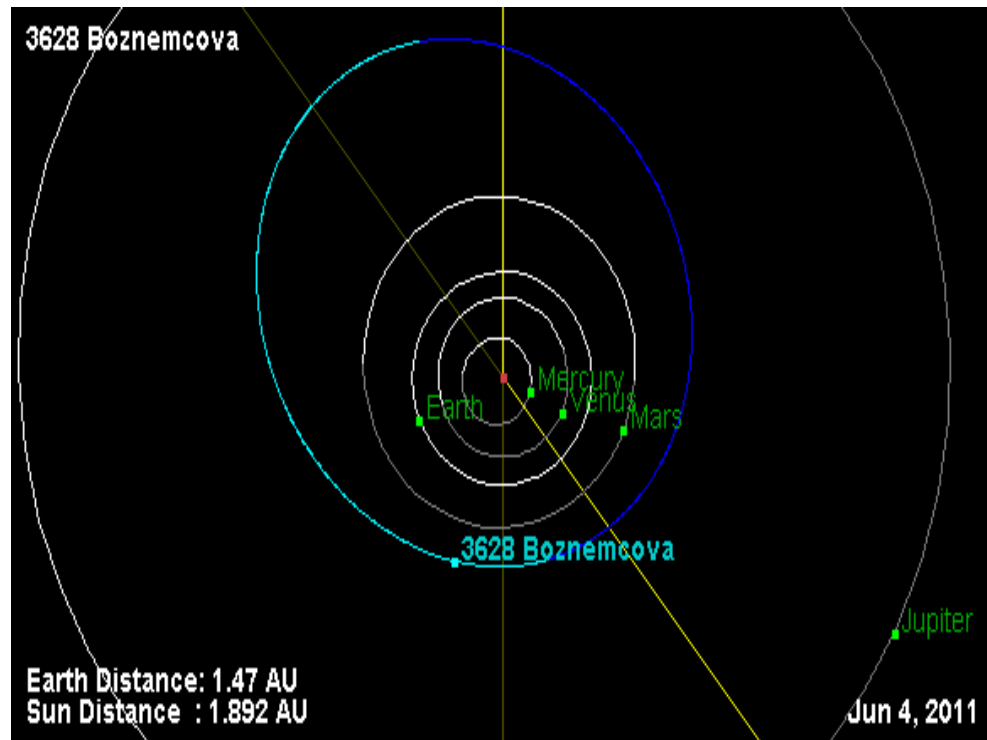
Owing to the less than favorable conditions under which 2002JB<sub>9</sub> was observed it would be beneficial to revisit this asteroid again. Extending the spectral coverage to the mid IR would also permit the detection of crystalline silica minerals on the surface. The existing spectral measurements of 3628 Božněmcová by Binzel et al (2007) and Hynes et al (2011) are quite noisy. A more confident determination of its surface mineralogy could

be made if data with a higher signal to noise ratio and extended spectral coverage to 2.7 um were available. Full rotational coverage would also be quite beneficial.

## Appendix I Orbits of asteroids 2002JB<sub>9</sub> and 3628 Božněmcová



- Semimajor axis = 2.716 AU
- eccentricity = 0.785
- inclination = 46.761°
- period = 4.48 years
- perihelion = 0.584 AU
- aphelion = 4.849 AU
- Mean anomaly = 49.136°
- longitude of the ascending node = 70.322°



- Semimajor axis = 2.539 AU
- eccentricity = 0.298
- $i = 6.884^\circ$
- period = 4.05 years
- $q = 1.782$  AU
- $Q = 3.298$  AU
- $M = 65.903^\circ$
- longitude of the ascending node =  $156.744^\circ$

## Appendix II Output from Pyroxene Calculator

Object: **3628 Boznemcova** BAR = **0.61**

Without corrections

| Wo     | Range(Fs) | BI Center | Eqn | Fs      | Range(Wo) | BII Center | Eqn |
|--------|-----------|-----------|-----|---------|-----------|------------|-----|
| 41.258 | Fs<10     | 1.02      | 2a  | 95.0756 | Wo<11     | 2.158      | 3a  |
| 48.424 | Fs10-25   | 1.02      | 2b  | 51.385  | Wo11-30   | 2.158      | 3b  |
| 46.378 | Fs25-50   | 1.02      | 2c  | 18.0618 | Wo30-45   | 2.158      | 3c  |
|        |           |           |     | 23.856  | Wo>45     | 2.158      | 3d  |

w/o  
BARcorr  
w/  
BARcorr

Select the values which satisfy both set of constraints

With BAR correction subtracted from Band I = **0.01367**

The correction factor (offset) can be obtained from the "BI Offset" sheet

NOTE: The correction should place the object on the pyroxene trend on the Band-Band plot

If the point plots below the pyroxene trend, this indicates an over-correction and the probable presence of an abundant calcic pyroxene (Cpx) component

| Wo        | Range(Fs) | BI Center | Eqn | Fs      | Range(Wo) | BII Center | Eqn |
|-----------|-----------|-----------|-----|---------|-----------|------------|-----|
| 36.502207 | Fs<10     | 1.00633   | 2a  | 95.0756 | Wo<11     | 2.158      | 3a  |
| 42.187746 | Fs10-25   | 1.00633   | 2b  | 51.385  | Wo11-30   | 2.158      | 3b  |
| 40.651637 | Fs25-50   | 1.00633   | 2c  | 18.0618 | Wo30-45   | 2.158      | 3c  |
|           |           |           |     | 23.856  | Wo>45     | 2.158      | 3d  |

Select the values which satisfy both set of constraints

This is the average pyroxene composition for single pyroxene or HED-like assemblages

Testing for possible Ordinary Chondrites

With H-chondrite High-Ca Px correction to Band II (-0.065 um +/- 0.018 um)

| Wo        | Range(Fs) | BI Center | Eqn | Fs      | Range(Wo) | BII Center | Eqn |
|-----------|-----------|-----------|-----|---------|-----------|------------|-----|
| 36.502207 | Fs<10     | 1.00633   | 2a  | 77.6426 | Wo<11     | 2.093      | 3a  |
| 42.187746 | Fs10-25   | 1.00633   | 2b  | 47.6475 | Wo11-30   | 2.093      | 3b  |
| 40.651637 | Fs25-50   | 1.00633   | 2c  | 18.9003 | Wo30-45   | 2.093      | 3c  |
|           |           |           |     | 31.526  | Wo>45     | 2.093      | 3d  |

Select the values which satisfy both set of constraints

Brearley and Jones p. 283-287

H-Chon Low-Ca Px

Fs14.5-18

H-Chon Augite

Fs7Wo45

H-Chon "Spectral" Wo

~6-7

If the calculated values do not fall in the H-Chondrite Low-Ca Opx and Wo range, the H-chondrite option can be eliminated

With L-chondrite High-Ca Px correction to Band II (-0.062 um +/- 0.007 um)

| Wo        | Range(Fs) | BI Center | Eqn | Fs      | Range(Wo) | BII Center | Eqn |
|-----------|-----------|-----------|-----|---------|-----------|------------|-----|
| 36.502207 | Fs<10     | 1.00633   | 2a  | 78.4472 | Wo<11     | 2.096      | 3a  |
| 42.187746 | Fs10-25   | 1.00633   | 2b  | 47.82   | Wo11-30   | 2.096      | 3b  |
| 40.651637 | Fs25-50   | 1.00633   | 2c  | 18.8616 | Wo30-45   | 2.096      | 3c  |



31.172      Wo>45      2.096      3d

Select the values which satisfy both set of constraints

Brearley and Jones p. 283-287

L-Chon Low-Ca Px      Fs19-22  
 L-Chon Augite      Fs8.5Wo45  
 L-Chon "Spectral" Wo      ~8-9

If the calculated values do not fall in the L-Chondrite Low-Ca Opx & Wo range, the L-chondrite option can be eliminated

**With LL-chondrite High-Ca Px correction to Band II (-0.076 um +/- 0.008 um)**

| Wo        | Range(Fs) | BI Center | Eqn | Fs      | Range(Wo) | BII Center | Eqn |
|-----------|-----------|-----------|-----|---------|-----------|------------|-----|
| 36.502207 | Fs<10     | 1.00633   | 2a  | 74.6924 | Wo<11     | 2.082      | 3a  |
| 42.187746 | Fs10-25   | 1.00633   | 2b  | 47.015  | Wo11-30   | 2.082      | 3b  |
| 40.651637 | Fs25-50   | 1.00633   | 2c  | 19.0422 | Wo30-45   | 2.082      | 3c  |
|           |           |           |     | 32.824  | Wo>45     | 2.082      | 3d  |

Select the values which satisfy both set of constraints

Brearley and Jones p. 283-287

LL-Chon Low-Ca Px      Fs22-26  
 LL-Chon Augite      Fs10Wo45  
 LL-Chon "Spectral" Wo      ~9-11

If the calculated values do not fall in the LL-Chondrite Low-Ca Opx & Wo range, the LL-chondrite option can be eliminated

**Object: Angra1**  
**Without corrections**

BAR = **0.41**

| Wo     | Range(Fs) | BI Center | Eqn | Fs      | Range(Wo) | BII Center | Eqn |  | BI          |
|--------|-----------|-----------|-----|---------|-----------|------------|-----|--|-------------|
| 48.216 | Fs<10     | 1.04      | 2a  | 103.658 | Wo<11     | 2.19       | 3a  |  | w/o BARcorr |
| 57.548 | Fs10-25   | 1.04      | 2b  | 53.225  | Wo11-30   | 2.19       | 3b  |  | w/ BARcorr  |
| 54.756 | Fs25-50   | 1.04      | 2c  | 17.649  | Wo30-45   | 2.19       | 3c  |  |             |
|        |           |           |     | 20.08   | Wo>45     | 2.19       | 3d  |  |             |

Select the values which satisfy both set of constraints

**With BAR correction subtracted from Band I = 0.073**

**The correction factor (offset) can be obtained from the "BI Offset" sheet**

**NOTE: The correction should place the object on the pyroxene trend on the Band-Band plot**

If the point plots below the pyroxene trend, this indicates an over-correction and the probable presence of an abundant calcic pyroxene (Cpx) component

| Wo      | Range(Fs) | BI Center | Eqn | Fs      | Range(Wo) | BII Center | Eqn |  |
|---------|-----------|-----------|-----|---------|-----------|------------|-----|--|
| 22.8193 | Fs<10     | 0.967     | 2a  | 103.658 | Wo<11     | 2.19       | 3a  |  |
| 24.2454 | Fs10-25   | 0.967     | 2b  | 53.225  | Wo11-30   | 2.19       | 3b  |  |
| 24.1763 | Fs25-50   | 0.967     | 2c  | 17.649  | Wo30-45   | 2.19       | 3c  |  |
|         |           |           |     | 20.08   | Wo>45     | 2.19       | 3d  |  |

Select the values which satisfy both set of constraints

This is the average pyroxene composition for single pyroxene or HED-like assemblages

**Testing for possible Ordinary Chondrites**

**With H-chondrite High-Ca Px correction to Band II (-0.065 um +/- 0.018 um)**

| Wo      | Range(Fs) | BI Center | Eqn | Fs      | Range(Wo) | BII Center | Eqn |
|---------|-----------|-----------|-----|---------|-----------|------------|-----|
| 22.8193 | Fs<10     | 0.967     | 2a  | 86.225  | Wo<11     | 2.125      | 3a  |
| 24.2454 | Fs10-25   | 0.967     | 2b  | 49.4875 | Wo11-30   | 2.125      | 3b  |
| 24.1763 | Fs25-50   | 0.967     | 2c  | 18.4875 | Wo30-45   | 2.125      | 3c  |
|         |           |           |     | 27.75   | Wo>45     | 2.125      | 3d  |

Select the values which satisfy both set of constraints

H-Chon Low-Ca Px Fs14.5-18 Brearley and Jones p. 283-287

H-Chon Augite Fs7Wo45

H-Chon "Spectral" Wo ~6-7

If the calculated values do not fall in the H-Chondrite Low-Ca Opx and Wo range, the H-chondrite option can be eliminated

**With L-chondrite High-Ca Px correction to Band II (-0.062 um +/- 0.007 um)**

| Wo      | Range(Fs) | BI Center | Eqn | Fs      | Range(Wo) | BII Center | Eqn |
|---------|-----------|-----------|-----|---------|-----------|------------|-----|
| 22.8193 | Fs<10     | 0.967     | 2a  | 87.0296 | Wo<11     | 2.128      | 3a  |
| 24.2454 | Fs10-25   | 0.967     | 2b  | 49.66   | Wo11-30   | 2.128      | 3b  |
| 24.1763 | Fs25-50   | 0.967     | 2c  | 18.4488 | Wo30-45   | 2.128      | 3c  |
|         |           |           |     | 27.396  | Wo>45     | 2.128      | 3d  |

Select the values which satisfy both set of constraints

L-Chon Low-Ca Px Fs19-22 Brearley and Jones p. 283-287

L-Chon Augite Fs8.5Wo45

L-Chon "Spectral" Wo ~8-9

If the calculated values do not fall in the L-Chondrite Low-Ca Opx & Wo range, the L-chondrite option can be eliminated

**With LL-chondrite High-Ca Px correction to Band II (-0.076 um +/- 0.008 um)**

| Wo      | Range(Fs) | BI Center | Eqn | Fs      | Range(Wo) | BII Center | Eqn |
|---------|-----------|-----------|-----|---------|-----------|------------|-----|
| 22.8193 | Fs<10     | 0.967     | 2a  | 83.2748 | Wo<11     | 2.114      | 3a  |
| 24.2454 | Fs10-25   | 0.967     | 2b  | 48.855  | Wo11-30   | 2.114      | 3b  |
| 24.1763 | Fs25-50   | 0.967     | 2c  | 18.6294 | Wo30-45   | 2.114      | 3c  |
|         |           |           |     | 29.048  | Wo>45     | 2.114      | 3d  |

Select the values which satisfy both set of constraints

LL-Chon Low-Ca Px      Fs22-26      Brearley and Jones p. 283-287

LL-Chon Augite      Fs10Wo45

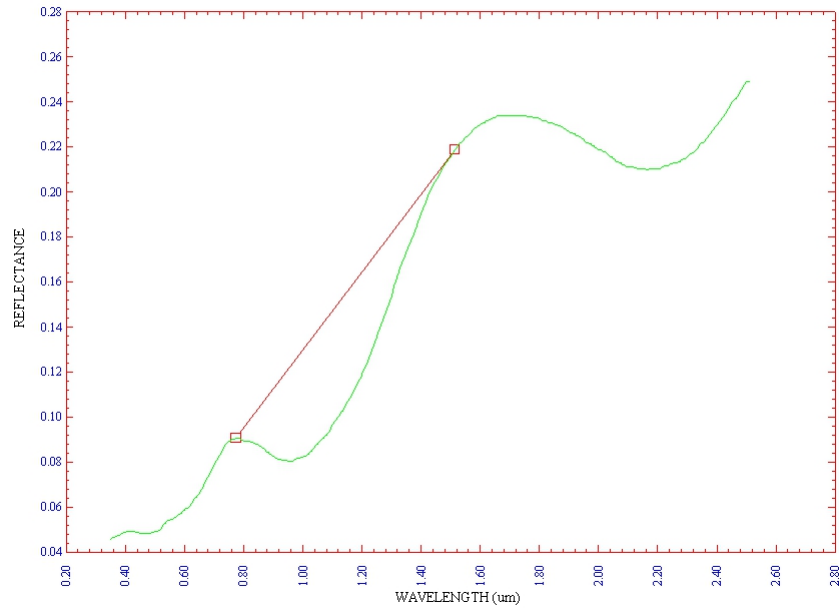
LL-Chon "Spectral"

Wo      ~9-11

If the calculated values do not fall in the LL-Chondrite Low-Ca Opx & Wo range, the LL-chondrite option can be eliminated

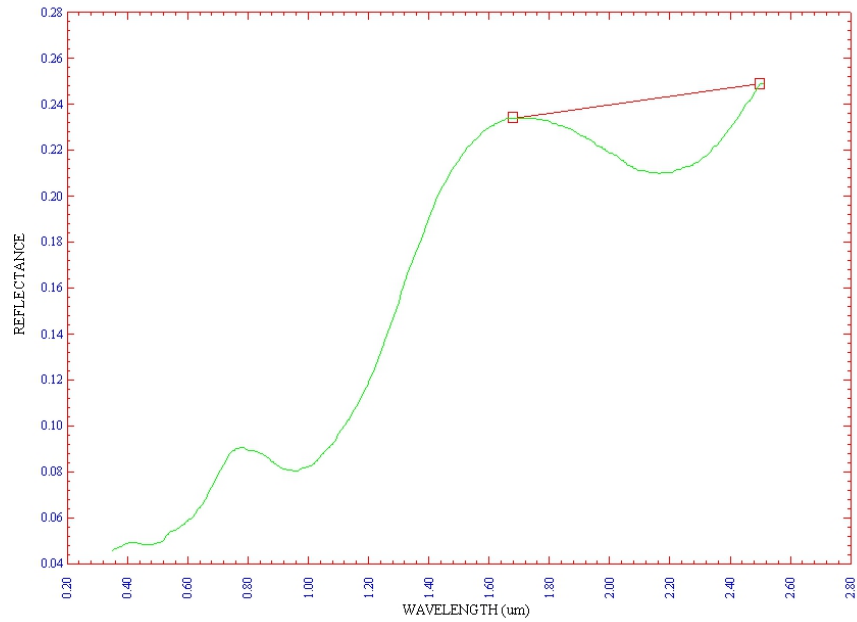
## Appendix III Continuum fits to Angra Dos Reis absorption features

Angra-Dos\_Reis Continuum Fit Band 1



Continuum Fit to band 1 absorption feature in Angra Dos Reis

Angra-Dos\_Reis Continuum Fit Band 2



Continuum Fit to band 2 absorption feature in Angra Dos Reis

## References Cited in this work

Adams, J.B. (1974) Visible and near-infrared diffuse reflectance spectra of pyroxenes as applied to remote sensing of solid objects in the solar system. *J. Geophys. Res.* 79, 4829-4836.

Alvarez L. W., W. Alvarez, F. Asaro, and H. V. Michel (1980) Extraterrestrial Cause for the Cretaceous-Tertiary Extinction. *Science* 208, 1095-1108.

Bancroft, G.M. and Burns, G.R. 1967 Interpretation of the electronic spectra of iron in pyroxenes. *Amer Min.*, 52, 1275-1277

Bell J.F., Owensby P. D., Hawke B. R. and Gaffey M. J. (1988) The 52-Color Survey: Final Results and Interpretation. *Abstracts of The Lunar and Planetary Science Conference*, Vol. 19 pp. 57

Bell, J.F., Izenberg, N.I., Lucey, P.G., Clark, B.E., Peterson, C., Gaffey, M.J., Joseph, J., Carcich, B., Harch, A., Bell, M.E., Warren, J., Martin, P.D., McFadden, L.A., Wellnitz, D., Murchie, S., Winter, M., Veverka, J.P., Thomas, M.S. Robinson, Malin, M., Cheng A., (2001) Near-IR Reflectance Spectroscopy of 433 Eros from the NIS Instrument on the NEAR Mission.: 1. Low phase angle observations. *Icarus*, 155, 119-144

Belskaya I.N., Shevchenko V.G. (2000) Opposition effect of asteroids. *Icarus* 147, 94-105

Bethe, H. A. (1929) Splitting of Terms in Crystals, *Ann. Physik*, 3, 133

Binzel, R.P., S. Xu, S.J. Bus, M.F. Skrutskie, M. Meyer, P. Knezek, and E.S. Barker (1993) The discovery of a main-belt asteroid resembling ordinary chondrite meteorites. *Science* 262, 1541-1543.

Binzel, R. P. and S. Xu (1993) Chips off of asteroid 4 Vesta: Evidence for the parent body of basaltic achondrite meteorites. *Science* 260, 186-191.

Binzel, R. P., Bus, S. J. Burbine, T. H. and Sunshine, J. M. (1996) Spectral properties of near-Earth asteroids: Evidence for sources of ordinary chondrite meteorites. *Science* 273, 946-948.

Bottke W. F., Jr., R. Jedicke, A. Morbidelli, J-M. Petit, and B. Gladman (2000) Understanding the Distribution of Near-Earth Asteroids. *Science* 288, 2190-2194.

Bottke, Rubincam & Burns (2000) Dynamical Evolution of Main Belt Meteoroids: Numerical Simulations Incorporating Planetary Perturbations and Yarkovsky Thermal Forces. *Icarus*, Vol. 145, no. 2, June 2000, Pages 301–331

Bottke W. F. Jr., D. Vokrouhlický, D. P. Rubincam, and D. Nesvorný (2006) The Yarkovsky and YORP Effects: Implications for Asteroid Dynamics. *Annu. Rev. Earth Planet. Sci.* 34, 157–191.

Brouwer, D., Van Woerkom, A.J.J (1950) *Astron. Papers U.S. Naval Obs.* **13**, 95

Bruton, D. (2006). "What were some of the effects of the collisions?" Frequently Asked Questions about the Collision of Comet Shoemaker–Levy 9 with Jupiter. Texas A&M University.

Burbine, T.H., McCoy, T.J; Binzel, R.P. (2001) Spectra of Angrites and Possible Parent Bodies. *Lunar and Planetary Science XXXII*

Burbine, T.H., McCoy, J.L, hinrichs, J.L. and Lucey, P.G. (2006) Spectral Properties of Angrites. *Meteoritics & Planetary Science* 41, Nr 8, 1139-1145

Burbine & Binzel (2002) Small Main-Belt Asteroid Spectroscopic Survey in the Near-Infrared

Burns, R. G. (1970) *Mineralogical Applications of Crystal Field Theory*. Cambridge Univ. Press. 224 pp.

Burns, R. G. (1993) *Mineralogical Applications of Crystal Field Theory - 2nd Ed.* Cambridge Univ. Press. 551 pp.

Burns, R. G. (1993) Origin of electronic spectra of minerals in the visible to near-infrared region. in *Remote Geochemical Analysis: Elemental and Mineralogical Composition* (C. M. Pieters and P. A. J. Englert, Eds.), pp. 3-29. Cambridge University Press, New York.

Bus S. J. and R. P. Binzel (2002) Phase II of the small main-belt asteroid spectroscopic survey - A feature based taxonomy. *Icarus* 158, 146-177.

Chapman, C.R., Johnson, T.V. and McCord, T.B. (1971) A Review of Spectrophotometric Studies of Asteroids. *Physical Studies of Minor Planets, Proceedings of IAU Colloq.* **12** 51-55

Chapman, C.R., D. Morrison, and B. Zellner (1975). Surface properties of asteroids: A synthesis of polarimetry, radiometry, and spectrophotometry. *Icarus* 25, 104-130.

- Chapman, C.R. and M.J. Gaffey (1979). Reflectance spectra for 277 asteroids. In *Asteroids* (T. Gehrels and M.S. Matthews, Eds.), University of Arizona Press, Tucson, pp. 655-687.
- Chesley S.R, Ostro, S.J, Vokrouhlick, D, Capek, D., Giorgin, J.D., Nolan, M.C., Margot, J.L., Hine, A.A., Benner, L.A.M and Chamberlin, A.B. (2003) Direct Detection of the Yarkovsky Effect by Radar Ranging to Asteroid 6489 Golevka. *Science* 5 December 2003:Vol. 302 no. 5651 pp. 1739-1742
- Chirikov, B.V. (1979) A universal instability of many-dimensional oscillator systems, *Phys. Rep.* 52: 263
- Cloutis E. A. (2002) Pyroxene reflectance spectra: Minor absorption bands and effects of elemental substitutions. *J. Geophys. Res. - Planets* 107(E6), 5039
- Cloutis E. A., Binzel, R.P., Burbine, T.H., Gaffey, M.J., McCoy, T.J. (2006) Asteroid 3628 Boznemcová: Covered with angrite-like basalts? *Meteoritics & Planetary Science* 41, Nr 8, 1147–1161
- Dell’Oro, A. & Cellino, A. (2007) The random walk of Main Belt asteroids: orbital mobility by non-destructive collisions. *Monthly Notices of the Royal Astronomical Society*, Vol. 380, Issue 1, pages 399–416.
- De Pater, I & Lissauer, J.J (2001) *Planetary Sciences*. Cambridge University Press
- Farinella P., Gonczi R., Froeschle Ch. and Froeschle C. (1993) The injection of asteroid fragments into resonances. *Icarus* 101, 174-187.
- Farinella, P., D. Vokrouhlicky, and W. K. Hartmann (1998) Meteorite delivery via Yarkovsky orbital drift. *Icarus* 132, 378–387.



- Farinella P. and Vokrouhlický D. (1999) Semimajor axis mobility of asteroidal fragments. *Science*, 283, 1507–1510.
- Froeschle, C.H, Scholl, H. (1986) The secular resonance  $\nu_6$  in the asteroid belt. *Astron. Astrophys.* 166, 326-332
- Gaffey M. J. (1986) The spectral and physical properties of metal in meteoritic assemblages: Implications for asteroid surface materials. *Icarus* 66, 468-486.
- Gaffey, M.J., J. F. Bell, R. H. Brown, T. H. Burbine, J. Piatek, K. L. Reed and D. A. Chaky (1993) Mineralogical variations within the S-type asteroid class. *Icarus* 106, 573-602.
- Gaffey M. J., E. A. Cloutis, M. S. Kelley and K. L. Reed (2002) Mineralogy of Asteroids. Book chapter, Asteroids III, University of Arizona Press.
- Gaffey M. J. (2010) Space Weathering and the Interpretation of Asteroid Reflectance Spectra. *Icarus* 209, 564-574.
- Gladman B. J., F. Migliorini, A. Morbidelli, V. Zappalà, P. Michel, A. Cellino, C. Froeschlé, H. F. Levison, M. Bailey and M. Duncan (1997) Dynamical lifetimes of objects injected into asteroid belt resonances. *Science* 277, 197-201.
- Gradie J. & Tedesco E. (1982) Compositional structure of the asteroid belt. *Science* 216, 1405-1407.
- Greenwood, R.C, Franchi, I.A., Jambon, A, Buchanan, P.C. (2005) Widespread magma oceans on asteroidal bodies in the early solar system. *Nature* 435 pp 916-918

Hardersen, P. S. (2003) Near-IR Reflectance Spectroscopy of Asteroids and Study of the Thermal History of the Main Asteroid Belt. Ph.D. Dissertation. Rensselaer Polytechnic Institute, Troy, New York. 411 pp.

Hardersen, P.S., Cloutis, E.A., Reddy, V., Mothe-Diniz, T., and Emery, J.P. (2011) The M-/X-asteroid menagerie: Results of an NIR spectral survey of 45 main-belt asteroids. *Meteoritics & Planetary Science* 46, Nr 12, 1910-1938

Hicks, M., Somers, J., Rhoades, H., McCormack, M., Gerhart, C., Bauer, J., Mainzer, A., Masiero, J., Grav, T. (2011) Broadband photometry of 267494 (2002 JB9): A near-Earth asteroid with remarkable solar phase behavior. *The Astronomers Telegram*

Kirkwood, D. (1876) On the distribution of the asteroids. Salem Press, MA

Lowry, S.C, Fitzsimmons, P., Pravec, P., Vokrouhlick, D., Boehnhardt, H., Taylor, P.A, Margot, J.L., Galad, A., Irwin, M., Irwin, J. and Kusnir, P.(2007) Direct Detection of the Asteroidal YORP Effect. *Science, Vol. 316 no. 5822* pp. 272-274

McCord, T.B., J.B. Adams, and T.V. Johnson (1970) Asteroid Vesta: Spectral reflectivity and compositional implications. *Science* 168, 1445-1447.

McFadden, L.A, Gaffey, J. and McCord, T.B (1985) Near-Earth Asteroids: Possible Sources from Reflectance Spectroscopy. *Science Vol. 229 no 4709* pp.160-163

McSween, H.Y., Jr. (1999) *Meteorites and Their Parent Planets 2<sup>nd</sup> Ed.* Cambridge University Press

Mittlefehldt, D.W., Kilgore, M. and Lee, M.T. 2002 Petrology and geochemistry of Sahara 99555 and the origin of angrites. *Meteoritics & Planetary Science* 37 pp 345-369

- Moons, M. and Morbidelli, A. (1995) Numerical Evidence on the Chaotic Nature of the 3/1 Mean Motion Commensurability. *Icarus* Vol. 115, Issue 1, May 1995, Pages 60–65
- Morrison, D. (2006) Asteroid and comet impacts: the ultimate environmental catastrophe. *Transactions of the Royal Society*, contribution to a discussion meeting on the issue: ‘Extreme natural hazards’.
- Morbidelli A., Jedicke R., Bottke W. F., Michel P., Tedesco E. F. (2002): From magnitudes to diameters: The albedo distribution of near Earth objects and the Earth collision hazard. *Icarus* 158, 329–342.
- Nakamura, T., Noguchi, T., Tanaka, M., Zolensky, M.E., Kimura, M., Tsuchiyana, A., Nakato, A., Ogami, T., Ishida, H., Uesugi, M., Yada, T., Shirai, K., Fujimara, A., Okazaki, R., Sandford, S.A., Ishibashi, Y., Masanao, A., Okada, Tatsuaki, O., Ueno, M., Mukai, T., Yoshikawa, M., Kawaguchi, J. (2011) Itokawa Dust Particles: A Direct link Between S-Type Asteroids and Ordinary Chondrites. *Science* Vol. 333 no 6046 pp. 1113-1116
- Öpik, E.J (1951) Collision Probabilities with the Planets and the Distribution of Interplanetary Matter. *Proceedings of the Royal Irish Academy*, Vol 54
- Petit, J.M., Morbidelli, A., Chamber, J. (2001) The Primordial Excitation and Clearing of the Asteroid Belt. *Icarus* 153, 338–347
- Rayner, J. T., Toomey, D. W., Onaka, P. M., Denault, A. J., Stahlberger, W. E., Vaca, W. D., Cushing, M. C., Wang, S. (2003) SpeX: A medium-resolution 0.8-5.5 micron

spectrograph and imager for the NASA Infrared Telescope Facility. *Publ. Astron. Soc. Pac.* 115, 362-382.

Rayner J. T., P. M. Onaka, M. C. Cushing and W. D. Vacca (2004) Four years of good SpeX. *SPIE 5492*, 1498-1509.

Rubincam, D. P. (2000) Radiative spin-up and spin-down of small asteroids, *Icarus* 148, 2-11.

Spitale, J. & Greenberg, R. (2002) Numerical Evaluation of the General Yarkovsky Effect: Effects on Eccentricity and Longitude of Periapse. *Icarus*, Vol. 156, Issue 1, pp. 211–222

Skrutskie, M.F., Cutri, R.M., Stiening, R., Weinberg, M.D., Schneider, S., Carpenter, J.M., Beichman, C., Capps, R., Chester, T., Elias, J. Huchra J., Liebert, J., Lonsdale, C., Monet, D.G., Price, S., Seitzer, P., Jarrett, T., Kirkpatrick, J.D., Gizis, J.E., Howard, E., Evans, T., Fowler, J., Fullmer, L., Hurt, R., Light, R., Kopan, E.L., Marsh, K.A., McCallon, H.L., Tam, R., Van Dyk, S. and Wheelock, S. (2006) The Two Micron All Sky Survey (2MASS). *The Astronomical Journal* 131 pp. 1163-1183

Taylor, P.A., Margot, J.L, Vokrouhilcky, D., Scheeres, D.J. (2007) Spin Rate of Asteroid (54509) 2000 PH5 Increasing Due to the YORP Effect, *Science* 13

Tisserand, M.F. (1882) *Ann. Obs Paris* 16 E1

Tedesco, E.F., J.G. Williams, D.L. Matson, G.J. Veeder, J.C. Gradie, and L.A. Lebofsky (1989) A three-parameter asteroid taxonomy. *Astron. J.* 97, 580-606.

- Tholen, D.J. (1984) *Asteroid Taxonomy from Cluster Analysis of Photometry*. PhD Dissertation, University of Arizona, Tucson, 150pp.
- Ustinova, Alexeev, & Gorin (2008) *Recently Fallen Bukhara (CV3) and Kilabo (LL<sup>^</sup>) Chondrites: A Parallel Study of Luminescence, Tracks, and Cosmogenic Radionuclides*. *Geokhimiya* No. 9 pp. 915-933
- Van Vleck, J. H. (1932) Theory of the Variations in Paramagnetic Anisotropy Among Different Salts of the Iron Group, *Phys. Rev.* 41, 208 - 215
- Warner, B. (2008) *Asteroid Lightcurve Analysis at the Palmer Divide Observatory - June - October 2007*. *Bulletin of the Minor Planets Section of the Association of Lunar and Planetary Observers*, Vol. 35, No. 2, p. 56-60
- Watson F.G. (1941) *Between the Planets*. Harvard Books on Astronomy, The Blakiston Company, Philadelphia, Penn., 222pp.
- Williams (1969) Secular perturbations in the solar system: Ph.D dissertation, University of California at Los Angeles
- Williams, J. G. (1971) Proper elements, families, and belt boundaries. In *Physical Studies of Minor Planets* (T. Gehrels, ed.), NASA SP-267, pp. 177-181.
- Williams J. G. (1973) Meteorites from the asteroid belt. *EOS (Trans. Am. Geophys. Union)* 54, 233.
- Williams J. G. and J. Faulkner (1981) The position of secular resonance surfaces. *Icarus* 46, 390-399.

Wisdom, J. (1982) *The Origin of the Kirkwood Gaps: A Mapping for Asteroidal Motion Near The 3/1 Commensurability*. *Astronomical Journal*, Vol 83 No. 3

Wisdom, J. (1983a) *Chaotic behavior and the origin of the 3/1 Kirkwood gap*. *Icarus* 56, 51-74.

Wisdom, J. (1983b) *Chaotic behavior near the 3/1 commensurability as a source of Earth crossing asteroids and meteorites*. *Meteoritics* 18, 422-423.

Wisdom, J. (1985) *A perturbative treatment of motion near the 3/1 commensurability*. *Icarus* **63**, 272-289.

Wisdom, J. (1985). *Meteorites may follow a chaotic route to Earth*. *Nature* 315, 731-733.

Wood and Kuiper (1963) *Photometric studies of asteroids*, *Astrophysical Journal*, vol. 137, p.1279

Xu S., R. P. Binzel, T. H. Burbine and S. J. Bus (1995) *Small main-belt asteroid spectroscopic survey: Initial results*. *Icarus* 115, 1-35.

Zellner, B., D.J. Tholen, and E.F. Tedesco (1985) *The eight-color asteroid survey: Results for 589 minor planets*. *Icarus* 61, 355-416